REPORT DOCUMENTATION PAGE	*Form Approved* *OMB No. 0704-0188*

1. REPORT DATE *(DD-MM-YYYY)* 02/29/2012	**2. REPORT TYPE** Final Report	**3. DATES COVERED** *(From - To)* 03/01/2009-02/29/2012

4. TITLE AND SUBTITLE **SINGLE-CYCLE OPTICAL PULSES AND** **ISOLATED ATTOSECOND PULSE GENERATION**	**5a. CONTRACT NUMBER** FA9550-09-1-0212
	5b. GRANT NUMBER
	5c. PROGRAM ELEMENT NUMBER
6. AUTHOR(S) Franz X. Kaertner	**5d. PROJECT NUMBER**
	5e. TASK NUMBER
	5f. WORK UNIT NUMBER
7. PERFORMING ORGANIZATION NAME(S) AND ADDRESS(ES) Massachusetts Institute of Technology, 77 Massachusetts Ave Cambridge, MA 02139	**8. PERFORMING ORGANIZATION REPORT NUMBER**
9. SPONSORING / MONITORING AGENCY NAME(S) AND ADDRESS(ES) Tatjana Curcic, Civ USAF AFMC	**10. SPONSOR/MONITOR'S ACRONYM(S)**
	11. SPONSOR/MONITOR'S REPORT NUMBER(S) AFRL-OSR-VA-TR-2012-0725

12. DISTRIBUTION / AVAILABILITY STATEMENT

Distribution A

13. SUPPLEMENTARY NOTES

14. ABSTRACT

The MIT Single-Cycle Pulse and Isolated Attosecond Pulse Generation Program enabled to demonstrate, for the first time, a novel pulse synthesis technology based on ultrabroadband multi-color OPCPAs and explore the generation and control of isolated attosecond XUV pulses using the synthesized pulses. We developed several relevant ultrafast laser technologies and attosecond measurement systems, such as picosecond cryo-cooled Yb:YAG pump laser amplifiers, 2D and 4DSI pulse characterization techniques, optical balanced cross-correlator, CEP-jitter measurement apparatus, adiabatic DFG technique for high-energy broadband seeding, and a FROG-CRAB setup for attosecond XUV pulse characterization. Experimental demonstration of HHG with the 2.1 μm source shows cutoff extension in Ar to 160 eV and promises the feasibility of coherent control of the HHG process with the synthesized sub-cycle electric-field transients after a further upgrade of the 800-nm OPCPA to the mJ level, as supported by our theoretical study. Since the scaling of energy and pulse duration is clearly possible by using higher-energy OPCPA pump lasers and/or by coherently adding different-color OPCPA systems, we believe that the high-energy pulse synthesis technology demonstrated under this grant has opened up a new high-energy ultrafast laser technology that is especially suited to attosecond and strong-field science.

15. SUBJECT TERMS

16. SECURITY CLASSIFICATION OF:			**17. LIMITATION OF ABSTRACT**	**18. NUMBER OF PAGES**	**19a. NAME OF RESPONSIBLE PERSON**
a. REPORT	**b. ABSTRACT**	**c. THIS PAGE**			**19b. TELEPHONE NUMBER** *(include area code)*

Standard Form 298 (Rev. 8-98)
Prescribed by ANSI Std. Z39.18

REPORT ON AFOSR CONTRACT# FA9550-09-1-0212
To: technicalreports@afosr.af.mil
Subject: Final Progress Statement to Dr. Tatjana Curcic

TITLE: SINGLE-CYCLE OPTICAL PULSES AND ISOLATED ATTOSECOND PULSE GENERATION

Mar. 2009- Feb. 2012, Final Report

Franz X. Kärtner

Massachusetts Institute of Technology,
Department of Electrical Engineering and Computer Science
and Research Laboratory of Electronics
Rm: 36-351, 77 Massachusetts Ave., Cambridge, MA 02139
Tel: 617 452-3616, Fax: 617 253-9611, email: kaertner@mit.edu

SINGLE-CYCLE OPTICAL PULSES AND ISOLATED ATTOSECOND PULSE GENERATION

I. Goals of project and summary of results achieved:

1. Goals of project

a) To demonstrate coherent sub-cycle pulse synthesis from a two-color optical parametric chirped pulse amplification (OPCPA) system generating over more than two octaves of bandwidth spanning the visible to the mid-IR.

b) To characterize the sub-cycle pulses using a two-dimensional spectral shearing interferometry (2DSI) technique and extend the technique to space-dependent measurement (4DSI).

c) To properly characterize the timing and phase jitter of the synthesized pulses.

d) To numerically and experimentally study the generation of isolated attosecond XUV pulses using the synthesized sub-cycle pulses with the photon energy up to 300 eV.

e) To optimize the attosecond pulse generation with synthesized pulses.

f) To develop an attosecond streaking interferometer based on frequency resolved optical gating for the complete reconstruction of attosecond bursts (FROG-CRAB) for characterization of attosecond pulses.

g) To develop a high-energy, kHz, picosecond pump laser for energy scaling of two OPCPA systems using cryogenically cooled Yb:YAG laser technology.

h) To implement the pump laser into OPCPA systems and experimentally demonstrate HHG.

2. Summary of Program Accomplishments:

2.1 Construction and characterization of a sub-cycle waveform synthesizer (Year 1 objectives)

- Development of ultrabroadband, carrier-envelope phase(CEP)-stable, few-cycle 2.1-μm and 800-nm OPCPAs
- First demonstration of coherent pulse synthesis from the two-color OPCPA outputs using a balanced optical cross-correlator (BOC)
- Characterization of the CEP stability of each few-cycle pulse using nonlinear spectral interferometry and the timing jitter between two pulses using BOC
- First demonstration of 2DSI technique for multi-octave spanning pulses and extension of the technique to the 4DSI scheme

2.2 HHG and attosecond pulse generation theoretical analysis (Years 2/3 objectives)

- Time-dependent Schrödinger equation (TDSE) simulations of isolated attosecond pulse generation with synthesized pulses
- Investigation of the features of HHG driven by sub-cycle optical pulses and optimization of attosecond pulse generation with CEP control

2.3 HHG and attosecond pulse generation experiments (Years 2/3 objectives)

- Demonstration of FROG-CRAB technique for attosecond pulse characterization
- Upgrade of 2.1-μm OPCPA using cryo-cooled Yb:YAG amplifier to mJ level
- HHG using the long-wavelength driver in Xe, Kr, and Ar: demonstration of cutoff extension (up to ~160 eV from Ar) and measurement of conversion efficiency
- Modification of 800-nm OPCPA for energy scaling
- High-energy seed generation for 2.1-μm OPCPA from adiabatic DFG technique

II. Detailed Description of Systems Constructed and Results Achieved

1. Construction and characterization of sub-cycle pulse synthesis based on two OPCPAs

Since the invention of mode-locked lasers, the ultrafast laser science community has seen tremendous progress towards better phase control, broader optical bandwidths, shorter pulse durations, and higher pulse energies. In recent years, the development of close-to-single-cycle, carrier-envelope phase (CEP) controlled high-energy optical pulses has already led to the generation of isolated attosecond pulses in the EUV range [1], expanding ultrafast spectroscopy to attosecond resolution [2]. However, further investigation and control of these physical processes demand even more from laser technology, simultaneously requiring full phase control, multi-octave-spanning bandwidth, and peak intensities of 10^{14} W/cm^2 and above. Such features would allow arbitrary shaping of the strong electric-field waveforms for steering ionized electron wavepackets [3] and precise control of tunneling and multiphoton ionization events.

Coherent synthesis of pulses with different spectra, or wavelength multiplexing, presents a route towards obtaining a multi-octave spanning laser spectrum. The benefit of this approach lies in its modular design and scalability in both bandwidth and pulse energy. Ultra-broadband optical parametric chirped pulse amplifier (OPCPA) is the most promising technology for producing wavelength-tunable, high-peak-power and high-average-power, few-cycle optical pulses with good pre-pulse contrast [4]. Ultrabroadband OPCPAs also maintain good CEP stability due to the low thermal load and the small dispersion required to stretch and compress the signals. Thus, OPCPA stands out as the ideal building module for high-energy pulse synthesis.

1.1 Single-cycle synthesizer based on multi-color broadband OPCPAs

Figure 1 shows a schematic of the system. It starts with an actively CEP-stabilized octave-spanning Ti:sapphire oscillator. The output of the oscillator is used to seed the two OPCPAs as well as the ytterbium-doped fiber amplifier (YDFA)/Nd:YLF hybrid CPA, which pumps the two OPCPAs. Outputs from the two OPCPAs are combined in a broadband neutral beamsplitter. A feedback loop based on a balanced optical cross-correlator (BOC) [5], allowing attosecond-precision relative timing stability, is implemented to ensure the coherent synthesis of the two pulses. Furthermore, the inclusion of an acousto-optic programmable dispersive filter (AOPDF) in each OPCPA allows independent spectral phase and amplitude adjustment of each pulse, enabling control and optimization of the synthesized waveform. Overall, a pulse energy of 15μJ is obtained with a bandwidth close to two octaves and the shortest high-field transient lasting only 0.8 cycles (amplitude FWHM) of the centroid frequency.

1.1.a) Ti:sapphire oscillator

The octave-spanning Ti:sapphire oscillator is pumped with 6W of 532 nm light, and it outputs an average power of 200mW with a repetition rate of 85MHz. The optical cavity is set up in an astigmatism-compensated x-folded geometry employing two concave double-chirped mirrors (DCMs) with 75mm radius of curvature. The dispersion of the Ti:sapphire gain crystal and the air within the cavity is precisely compensated by DCM pairs, a BaF_2 plate, and a BaF_2 wedge pair. BaF_2's low ratio of the group-delay dispersion and the third-order dispersion allows the design of octave-spanning DCMs with 99.9% reflectivity from 580nm to 1200nm. Finally, a broadband quarter-wave $ZnSe/MgF_2$ output coupler (OC) that transmits more on the spectral edges than the center helps reshape the output spectrum to achieve a bandwidth of an octave. Figure 2b reports the output spectrum of the oscillator, showing the octave is reached at the spectral density of -25dB.

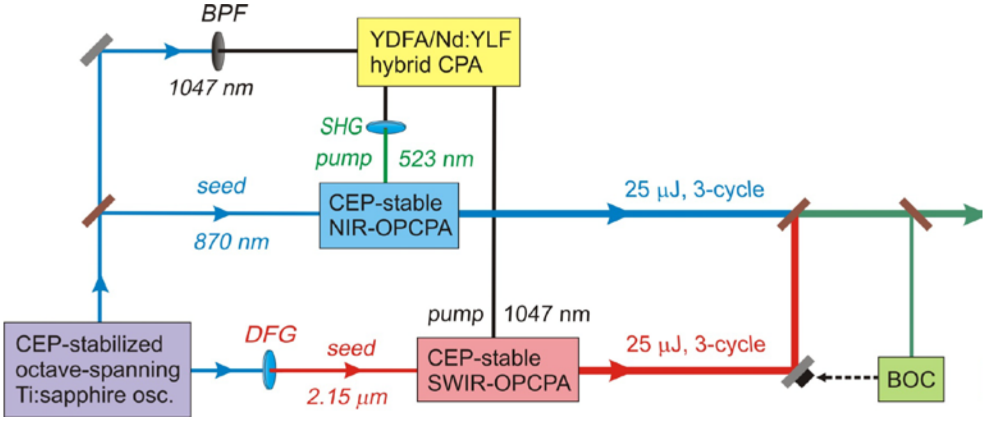

Figure 1. Two CEP-stabilized, few-cycle OPCPAs centered at different wavelengths are coherently synthesized to produce isolated high-energy non-sinusoidal optical waveforms at 1-kHz repetition rate. A BOC-assisted feedback loop allows attosecond-precision relative timing stability and ensures the coherent synthesis of the two OPCPA pulses. Full control over the optical phase, enabled by the inclusion of an AOPDF in each OPCPA, allows for any optical waveform given the amplified spectrum. BOC: balanced optical cross-correlator; YDFA: Ytterbium-doped fiber amplifier; SHG: second-harmonic generation; DFG: difference-frequency generation; BPF: bandpass filter.

The output of the oscillator is split in a dichroic mirror (DM) that transmits the light from 650 to 1050nm and reflects the light below 650nm and above 1050nm. The transmission port is used for seeding the rest of the system, and the reflection port is directed into an *f*-2*f* self-referencing interferometer for locking the CEP of the oscillator. A collinear configuration is chosen for its robustness against environmental noise. Six bounces on DCMs are employed for proper group-delay adjustment to maximize the CEP-beat signal. After the DCM-based delay line, the beam is focused onto a 1-mm-thick type I β-barium borate (BBO) crystal for second-harmonic generation (SHG). The emitted SHG light and the fundamental light are spatially filtered using an iris diaphragm, spectrally filtered using a 10-nm interference bandpass filter (BPF) centered at 570nm, and directed to a fast avalanche photodiode (MenloSystems, APD210). The CEP-offset frequency is locked to a fourth of the oscillator's repetition rate through a phase-locked loop that feeds back to an acousto-optic modulator (AOM) regulating the pump power, thus shifting the CEP-offset frequency. A digital phase detector (DPD) is used to increase the capture range (±32π) beyond a traditional analog mixer (±π/2). Figure 2c shows the power spectral density (PSD) of the residual CEP fluctuations and the integrated CEP r.m.s.

phase error (10Hz to 1MHz) is 60mrad. Since the major source of CEP is the intracavity intensity fluctuations introduced by pump laser noise, the phase noise rapidly decays beyond the relaxation frequency that is typically a few hundred kHz. Therefore, the upper limit of the measurement is set to be 1 MHz to exclude the high-frequency noise contributed by the electronics noise floor rather than the laser phase noise itself.

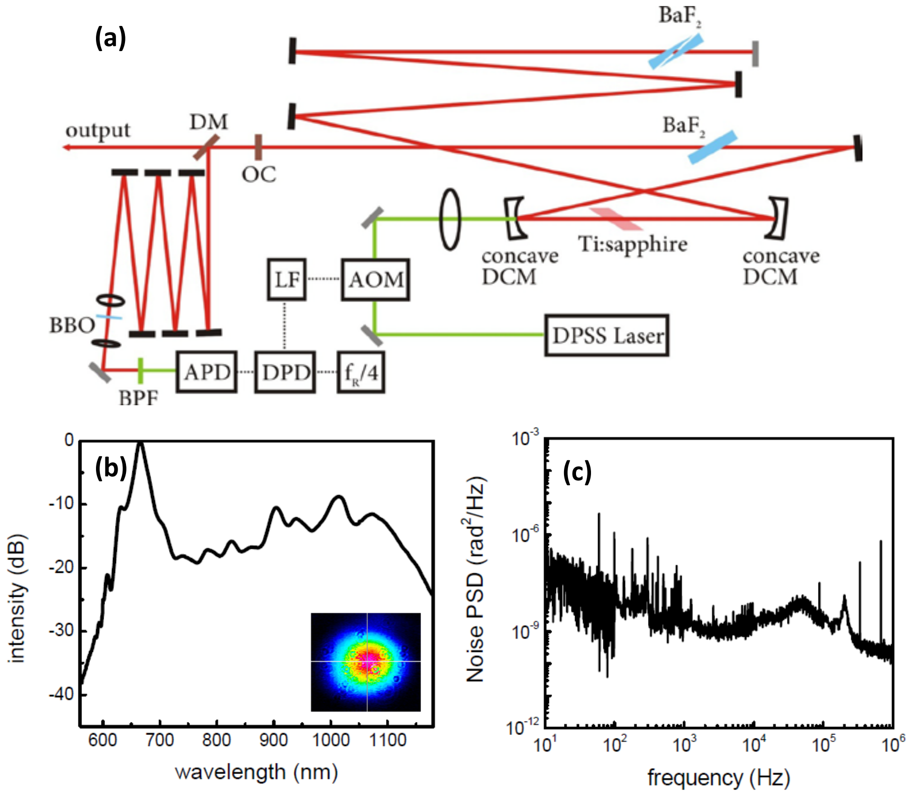

Figure 2. (a) Scheme of the CEP-stabilized octave-spanning Ti:sapphire oscillator. DM: dichroic mirror; OC: output coupler; DCM: double-chirped mirror; DPSS laser: diode-pumped solid-state laser; BPF: bandpass filter; APD: avalanche photodiode; DPD: digital phase detector; LF: loop filter; AOM: acousto-optic modulator. All DCMs are colored in black and all silver mirrors are colored in gray. (b) The output spectrum of the oscillator. The lower inset is the output beam profile. (b) The power spectral density (PSD) of the oscillator's residual CEP fluctuation. The integrated phase noise is 60 mrad.

1.1.b) Seed and pump for OPCPA

Figure 3a shows the all-optical synchronized seed and pump generation scheme. A broadband 10/90 beamsplitter divides the oscillator output into two parts: 10% of the oscillator output is directed to the NIR-OPCPA channel centered around 870-nm while the rest of the output is focused into a 2 mm MgO-doped periodically poled congruent lithium niobate (MgO:PPcLN) crystal with a poling period of 13.1 μm, wherein intrapulse difference-frequency generation (DFG) creates 2.15-μm seed pulses for the SWIR-OPCPA channel. Figures 3b and 3c are the spectrum of the two seeds, both reaching a bandwidth of more than half an octave (full width at -20dB).

After the intrapulse DFG stage, a DM and a 4-nm BPF is used to pick up the 1047nm component for seeding the YDFA/Nd:YLF hybrid CPA, which pumps the two OPCPAs. To suppress amplified spontaneous emission in the Nd:YLF regenerative amplifier (RGA), the seed is pre-amplified to 3 pJ in two YDFAs. The gain of the YDFAs is kept to 10 to avoid parasitic lasing at 1030nm. The Nd:YLF CPA system consists sequentially of a chirped fiber Bragg grating (CFBG) stretcher, a Nd:YLF RGA followed by two Nd:YLF multi-pass slab amplifiers (MPSA), and a diffraction grating compressor. The CFBG has a length of 10 cm, super-Gaussian apodization and a chirp rate of 440 ps/nm. The grating was inscribed in Nufern PS1060 photosensitive fiber using a phase-mask scanning technique in a Sagnac interferometric configuration. The pulse duration after the Nd:YLF RGA is 110 ps with a bandwidth of 0.25 nm, enough to avoid B-integral-related damage in the Nd:YLF MPSAs.

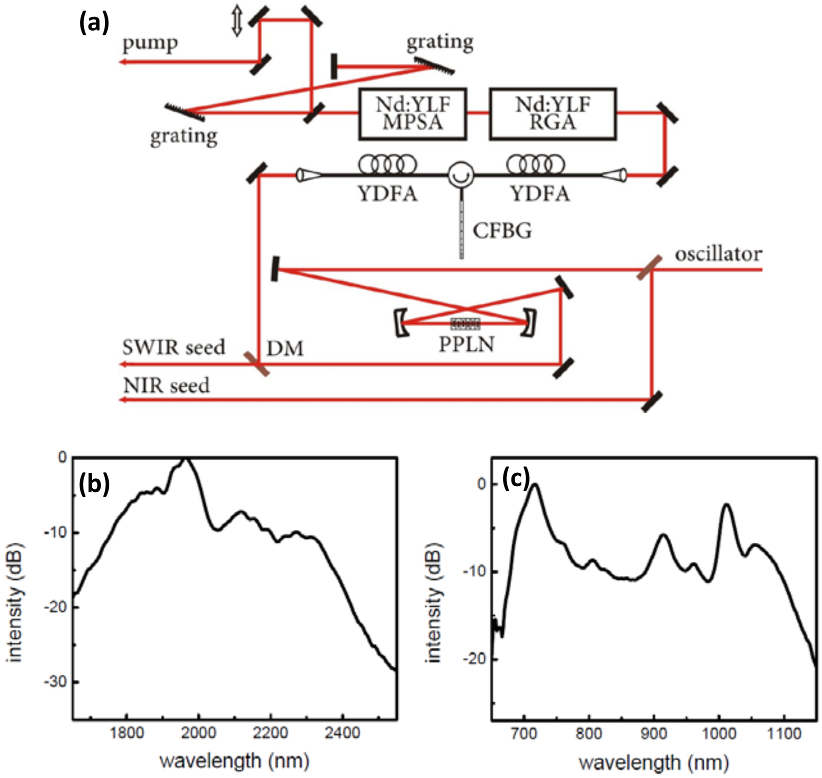

Figure 3. (a) Scheme of the all-optical-synchronized seed and pump generation. 10% of the oscillator output is used to seed the NIR-OPCPA channel while the rest of the output is focused into a 2 mm MgO-doped PPLN crystal, wherein intrapulse DFG creates 2.15-μm seed pulses for the SWIR-OPCPA channel. After the intrapulse DFG stage, a dichroic mirror (DM) is used to pick up the 1047-nm component for seeding the YDFA/Nd:YLF hybrid CPA, which pumps the two OPCPAs. The CFBG has a chirp rate of 440 ps/nm, enough to avoid B-integral-related damage in the Nd:YLF regenerative amplifier (RGA) and the two multi-pass slab amplifiers (MPSAs). (b) The seed spectrum of the SWIR-OPCPA. (c) The seed spectrum of the NIR-OPCPA.

Figure 4 shows the schematics of the Nd:YLF RGA (High-Q Laser) and the Nd:YLF MPSAs (Q-Peak). All Nd:YLF crystals are oriented to operate at the 1047nm emission line, utilizing the high gain quality. In the RGA, the Nd:YLF crystal is back-coated such that the 1047nm light is reflected while the 798nm diode pump is transmitted. A quarter waveplate (QWP), a Pockels cell (PC) operating at 0^o and π/4, and a thin-film polarizer (TFP) control the injection and ejection of the RGA pulses. The total cavity length is 1.5m. To reduce the loss associated with the thermal lensing, a quasi-CW pumping scheme is employed: the crystal is pumped for 450μs until the seed is injected. A single-pass small-signal gain of 2 can be achieved and the RGA output energy is 1.05mJ with a shot-to-shot r.m.s. energy fluctuation better than 0.5%. The overall RGA gain is more than 90dB and the output bandwidth is reduced to 0.25nm due to the strong gain narrowing. The RGA output pulse is then further amplified in the two three-pass Nd:YLF MPSAs. Each Nd:YLF crystal is 28 mm long, 2 mm by 6 mm in aperture, and side pumped with 78 W optical power. Due to the side pumping geometry, the asymmetric thermal lensing introduces astigmatism to the output pulse. A telescope with tilted lenses and cylindrical lenses is thus implemented after each MPSA to correct the astigmatism. Overall, the two Nd:YLF MPSAs offer a gain of 6.3 and an output pulse energy of 5.7 mJ is obtained. The pulse is then compressed using a gold-coated grating pair, where the gratings have a groove density of 1800 lines/mm and a diffraction efficiency of 90%. The separation between the two gratings is set to 2.7 m with multiple bounces off dielectric mirrors to achieve a compact setup. The throughput of the diffraction grating compressor is ~65% and a compressed pulse duration of 12 ps (~1.3x of the transform limit) is measured using a single-shot autocorrelator. A half waveplate and a polarization beamsplitter then divides the pulse into two parts where 1mJ is used to pump the SWIR-OPCPA and 2mJ is first frequency doubled in a 1cm lithium triborate crystal before being used to pump the NIR-OPCPA. The frequency doubling process has a conversion efficiency of ~45% and further push to higher conversion is undesirable due to the loss of beam quality.

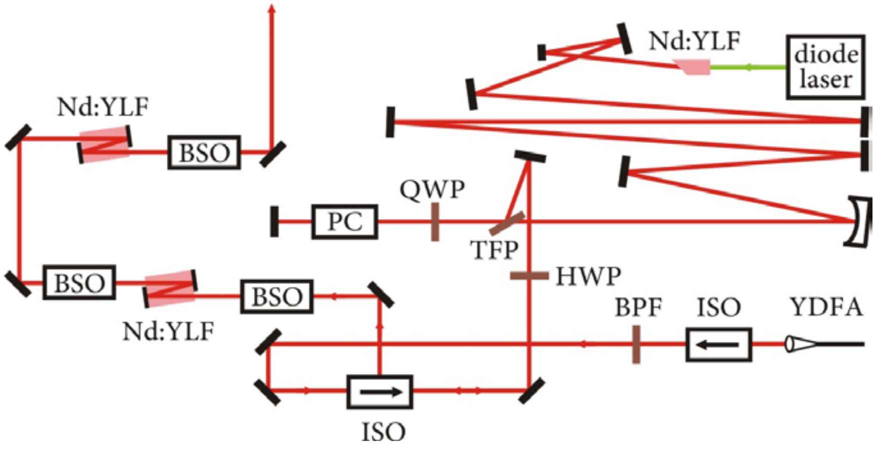

Figure 4. Scheme of the Nd:YLF hybrid chirped pulse amplifier, including a regenerative amplifier (RGA) and two Nd:YLF multi-pass slab amplifiers (MPSAs). The RGA output energy is 1.05mJ with a shot-to-shot r.m.s. energy fluctuation better than 0.5% and the output bandwidth is 0.25 nm. The RGA output pulse is then further amplified in the two three-pass Nd:YLF MPSAs. Overall, the two Nd:YLF MPSAs offer a gain of 6.3 and an output pulse energy of 5.7 mJ is obtained. YDFA: ytterbium-doped fiber amplifier; ISO: optical isolator; BPF: bandpass filter; HWP: half waveplate; TFP: thin film polarizer; QWP: quarter waveplate; PC: Pockels cell; BSO: beam shaping optics.

For the stable operation of OPCPAs, pump and signal pulses must be synchronized to within less than a fraction of their durations. Employment of picosecond pumps, which are advantageous over nanosecond pumps in terms of gain-bandwidth product, thus precludes the use of electronic synchronization methods. Thanks to the octave-spanning spectrum of the Ti:sapphire oscillator, direct seeding of a YDFA/Nd:YLF hybrid CPA is possible and thus the pump and signal are optically synchronized. A study of the optical synchronization scheme [6] shows that the residual timing jitter and drift over an hour are well below 1ps, less than 10% of our pump duration. Day-to-day timing shift between the pump and signal pulses has been observed, but the amount of shift can be easily accommodated by tuning the optical delay line of the pump.

1.1.c) Optical parametric chirped pulse amplifiers

Figure 5 shows the modular schematics of both OPCPAs. The signal is first stretched by Stretcher-1 to 40-50% of the pump pulse duration and then pre-amplified in the first OPCPA stage to 1-2 μJ with a gain of 50-60dB. The pre-amplified pulse is further stretched to 70-80% of the pump pulse duration by the Stretcher-2 and finally the signal is amplified to 20-30 μJ with a gain of 20-30dB. Of note, the gain of the pre-amplifier and the power-amplifier are significantly different and thus the stretching ratios for the signal have to be different for simultaneously optimizing energy conversion, amplification bandwidth, and signal-to-noise ratio. Between the two OPCPA stages, a fine phase management setup (for example, the AOPDF in our system) and a spatial filter for mode cleaning and superfluorescence suppression are included. While the fine phase management setup enables control and optimization of the synthesized waveform, it inevitably introduces signal loss and thus it is generally better to place it between the pre-amplifier and the power-amplifier for simultaneous optimization of output power and superfluorescence suppression: If placed before the pre-amplifier, its losses directly reduce the signal-to-noise ratio, which is set by the ratio of seed power to equivalent noise energy in vacuum modes. Placed after the power-amplifier, its losses reduce the output power. An effective spatial filter, created by setting the pump beam width less than a half of the signal beam width and placing the nonlinear crystal a few diffraction lengths away from the signal focus, improves the beam quality and eliminates the phase-matched, superfluorescence-dominated high-order spatial modes of the signal. If the initial signal-to-noise ratio is particularly low, such as for our SWIR-OPCPA, an additional iris diaphragm is implemented for the same purpose. At the end, a bulk material is used to compress the pulses to their transform limit.

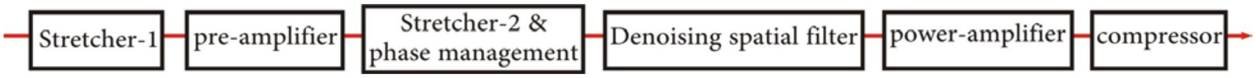

Figure 5. Modular scheme of the two-stage OPCPA. The signal is first stretched by the Stretcher-1 and then pre-amplified in the first OPCPA stage. The pre-amplified pulse is further stretched by the Stretcher-2 and finally amplified in the second OPCPA stage. Between the two OPCPA stages, a phase management setup and a spatial filter for mode cleaning and superfluorescence suppression are included. At the end, a bulk material is used to compress the pulses.

For the SWIR-OPCPA, a 30-mm bulk silicon block is used as the Stretcher-1 to stretch the signal to 5 ps. The signal is pre-amplified to 1.5 μJ in a 3-mm MgO:PPcLN with a poling period of 31.0 μm, pumped with 150 μJ pulses. The pre-amplified pulse is further stretched to 9.5 ps by an AOPDF which also serves as a fine phase management setup. Of note, the AOPDF can also shape the output spectrum but care has to be taken to ensure sufficient seed energy for the power-amplifier. The gain medium for the power-amplifier is a 3-mm MgO-doped periodically poled stoichiometric lithium tantalate crystal (MgO:PPsLT) with a poling period of 31.4 μm, pumped with 750 μJ pulses. The output pulses have 25 μJ energy and can be compressed to nearly transform-limited 24 fs duration in a 300-mm broadband anti-reflection coated Suprasil-300 glass block. For the NIR-OPCPA, a Brewster prism pair with 1-m apex-to-apex distance stretches the signal to 5 ps. The signal is pre-amplified to 2 μJ in a double-pass, non-collinear (2.4° pump-signal angle) geometry in a type-I, 5-mm-long BBO crystal cut at $\theta=24°$, and pumped with 250 μJ pulses. The pre-amplified pulse is further stretched to 6.2 ps by a combination of a Treacy grating pair and an AOPDF. The gratings have a groove density of 300 lines/mm and the separation between the two gratings is 82 mm. The Treacy grating pair is included in order to balance the excess high-order dispersion introduced by the Brewster prism pair. Additionally, the CEP drift caused by a Treacy grating pair due to temperature fluctuation is opposite in sign to that of a Brewster prism pair [7] and thus the inclusion of a Treacy grating pair improves the long-term CEP stability. Again the AOPDF also serves as a fine phase management setup here. The gain medium for the power-amplifier is the same as the first OPCPA stage, but pumped with 650 μJ pulses. The output pulses with an energy of 25 μJ are then compressed to 9 fs in a 40-mm Brewster-cut N-LaSF9 glass block.

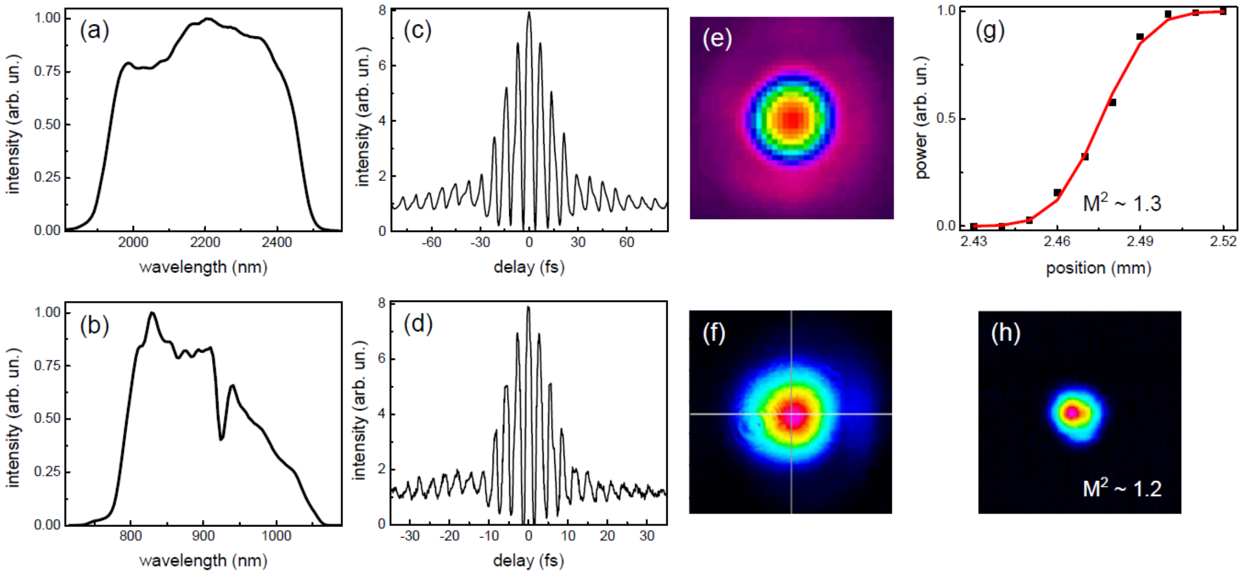

Figure 6. (a) The output spectrum of the SWIR-OPCPA. (b) The output spectrum of the NIR-OPCPA. (c) The interferometric autocorrelation trace of the SWIR-OPCPA pulses. (d) The interferometric autocorrelation trace of the NIR-OPCPA pulses. (e) The far-field beam profile of the SWIR-OPCPA. (f) The far-field beam profile of the NIR-OPCPA. (g) The knife-edge measurement of the near-field beam profile of the SWIR-OPCPA, indicating a M^2 value of 1.3. (h) The near-field beam profile of the NIR-OPCPA, indicating a M^2 value of 1.2.

Figures 6 and 7 show the characterization of the two OPCPAs. Both OPCPAs reach bandwidths of more than half an octave (full width at -20dB) and the combined spectrum spans over 1.8 octaves. The OPCPA outputs can be both compressed to within 10% of their transform-limited pulse durations, measured with interferometric autocorrelators (Figures 6c and 6d). Figures 6e to 6h show the near-field and far-field beam profiles, showing clean fundamental Gaussian modes with good M^2 values. As the CEP-offset frequency of the Ti:sapphire oscillator is locked to one fourth of its own repetition rate and the same frequency is used as the master clock of the whole system, the CEP of the NIR-OPCPA is actively stabilized. On the other hand, the CEP of the SWIR-OPCPA is in addition passively stabilized due to the intrapulse DFG process used to produce the seed. Using an *f*-3*f* interferometer and five-shot integration, the CEP stability of the SWIR-OPCPA was verified with an r.m.s. fluctuation of 127 mrad (Figure 7a). An *f*-2*f* interferometer with five-shot integration was used to verify the CEP stability of the NIR-OPCPA, which shows an r.m.s. fluctuation of 135-mrad (Figure 7b). CEP stabilization of both OPCPAs is an important first step toward the coherent synthesis. Its role and the effect of the residual fluctuations will be discussed in the following sections.

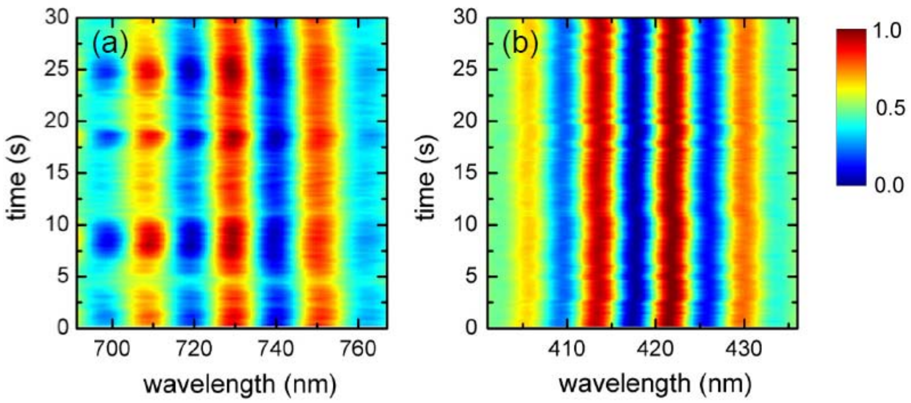

Figure 7. (a) *f-3f* inteferogram of the SWIR-OPCPA with 5-shot integration over 30 seconds, measuring an r.m.s. CEP fluctuation of 127 mrad. (b) *f-2f* inteferogram of the NIR-OPCPA with 5-shot integration over 30 seconds, measuring an r.m.s. CEP fluctuation of 135 mrad.

1.1.d) Coherent pulse synthesis

Outputs from the two OPCPAs are individually collimated with the diameter of the SWIR-OPCPA 2.5 times larger than that of the NIR-OPCPA and then combined in a broadband neutral beamsplitter. When focused, the two beams at the focus have the same spot size and this "constant waist width" configuration offers the unique property that the temporal pulse form remains unchanged upon propagation, whereas distortion appears in the near-field when the "constant diffraction length" configuration is used [8]. The overall spectrum spans over 1.8 octaves and the energy of the synthesized pulse is 15 μJ.

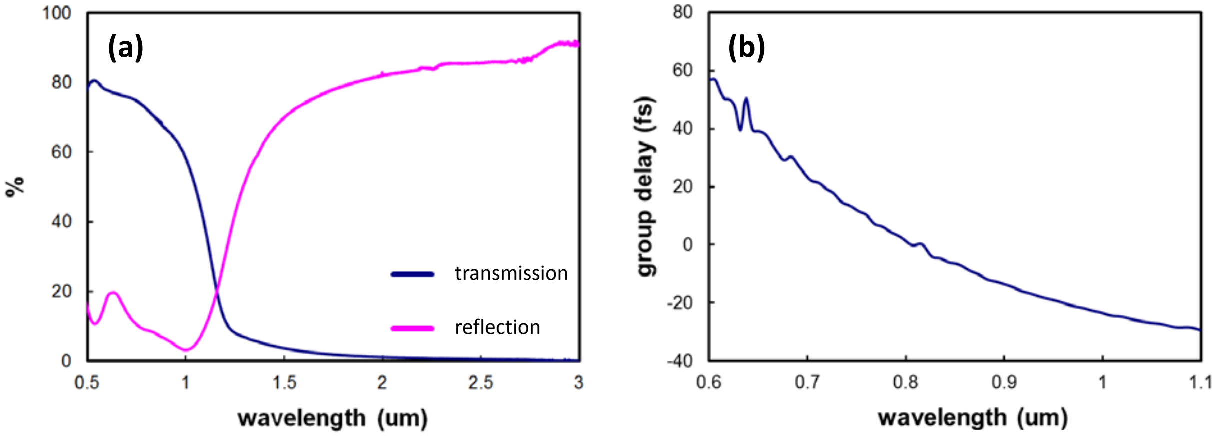

Figure 8. (a) Transmission and reflection characteristics of an ITO dichroic mirror. (b) Dispersion characteristics of an ITO dichroic mirror in the near-IR regime where the light is transmitted.

The outputs of the two OPCPAs are combined in a broadband neutral beamsplitter, which introduces 25% energy loss. In addition, only half of the synthesized pulse energy is available for experiments because the other half is directed to the BOC. Since the pulse energy directed to the BOC is much more than is needed, a custom-made dichroic mirror can be implemented to improve the experimentally available pulse energy by a factor of >2. Figure 8 shows the characterization of the indium-tin-oxide (ITO) dichroic mirror. It is transparent in the visible to near-IR regime, but behaves like a metallic mirror in the mid-IR regime. The dispersion in the near-IR regime is small and smooth such that it can be compensated with the AOPDF. With this new dichroic mirror, the energy of the pulse synthesizer can be improved by a factor of >2.

The phase coherence between the two OPCPA pulses is ensured by the following procedure (Figure 9): we first ensure stabilization of the CEPs of the NIR-OPCPA pulses (φ1) and SWIR-OPCPA pulses (φ2) (see Figure 7), and then stabilize the relative timing between the two OPCPA pulses (Δt). Precise stabilization of these three parameters is required for coherent synthesis of the two OPCPA pulses, and subsequent control of each parameter allows precise waveform shaping.

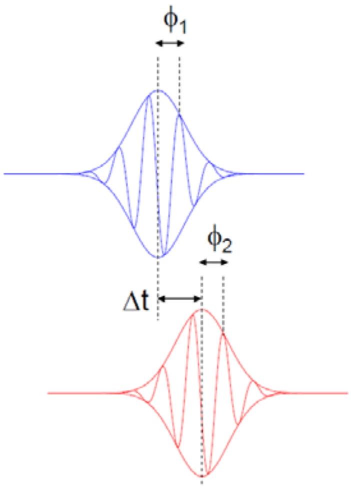

Figure 9. Cartoon showing a way to establish the phase coherence between the two OPCPA pulses. The CEPs of the NIR-OPCPA pulses (φ1) and the SWIR-OPCPA pulses (φ2) are first stabilized independently and then the relative timing between the two OPCPA pulses (Δt) is stabilized. Precise stabilization of these three parameters is required for coherent synthesis of the two OPCPA pulses, and subsequent control of each parameter allows precise waveform shaping.

As described in the previous section, the CEP of the SWIR-OPCPA is passively stabilized up to residual r.m.s. fluctuations of 127 mrad while the CEP of the NIR-OPCPA is actively stabilized to within a r.m.s. fluctuation of 135 mrad. To stabilize the relative timing, a feedback loop based on a BOC is implemented. A BOC is the optical equivalent of a balanced microwave phase detector and is particularly suitable for measuring slow timing drifts with attosecond precision because the balanced detection configuration cancels the amplitude noise. Figure 10a shows the schematics of the BOC. One part of the combined beam is directed to the BOC which consists of two nearly identical cross-correlators using 200-µm-thick BBO crystals, phase matched for sum-frequency generation (SFG) of 870-nm light and 2.15-µm light. Use of the SWIR-OPCPA delay stage and a 4-mm-thick calcium fluoride (CaF_2) window between cross-correlators sets the group delay between pulses to +25 fs in one cross-correlator and -25 fs in the other. An additional ~2-mm-thick calcium fluoride window ensures zero group delay (Δt = 0.0 fs) between both pulses at the combined output. For deviations from this zero-delay configuration of up to ±20 fs, the photodetector signal is linearly proportional to the time difference and thus can be used as the error signal fed to the loop filter in the feedback system (Figure 10b). Furthermore, in the vicinity of the zero crossing, the setup delivers a balanced signal and thus the amplitude noise of each OPCPA output does not affect the detected error signal. Since the balanced operation is key to attosecond precision, it is thus not desirable to offset the locking point as the mechanism to change the relative timing (Δt). Instead, the wedge pair in the path to the BOC should be used to change the relative timing (Δt) without offsetting the locking point and introducing additional dispersion to the combined output.

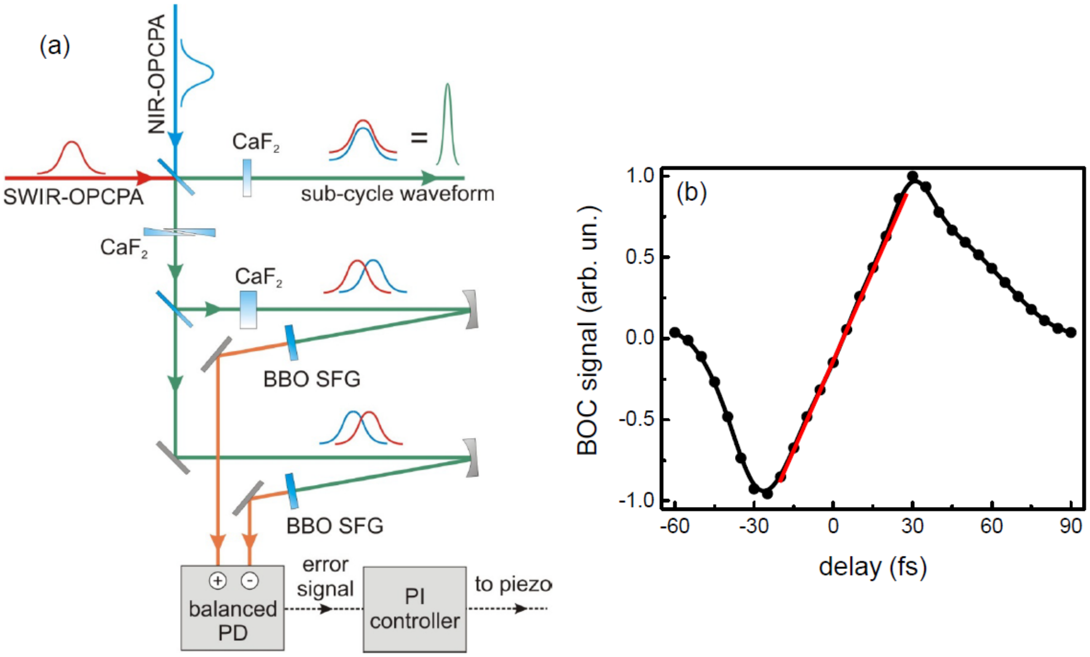

Figure 10 (a) Scheme of the BOC-assisted feedback loop for the stabilization of the relative timing. (b) BOC signal as a function of the relative timing between the two OPCPA pulses. The red line indicates the linear operation regime. BOC: balanced optical cross-correlator; SFG: sum-frequency generation; PD: photodetector.

Since the OPCPAs and pump laser system are all seeded by a single octave-spanning Ti:sapphire oscillator, the two OPCPA pulses are already synchronized to within environmental fluctuations. Freely running, the system displays a peak-to-peak relative timing drift of 30fs over a measurement time of 10s, with the main noise contribution below 30-Hz (Figure 11). Feedback control of the SWIR-OPCPA's path length over a bandwidth of 30 Hz reduces the relative timing drift to 250 as, less than 5% of the oscillation period of the SWIR-OPCPA (7.2 fs).

Since these three parameters (the CEP of the NIR-OPCPA, φ1, the CEP of the SWIR-OPCPA, φ2, and the relative timing between the two OPCPAs, Δt) significantly influence the synthesized electric-field waveform, it is important to make sure that the residual jitter is sufficiently small to impart only a negligible effect. Figure 12 shows the synthesized electric-field waveform with the r.m.s. value of each residual jitter added to the respective parameters (black dotted line) superimposed with the unperturbed waveform (green solid line). To quantify the waveform difference, we calculate the relative squared error (RSE) in a 10-fs time window that covers the main pulse as well as the two satellite pulses. Currently the 250-as relative timing jitter results in the largest waveform change (2.22% RSE), but it can be further reduced using a broader feedback bandwidth.

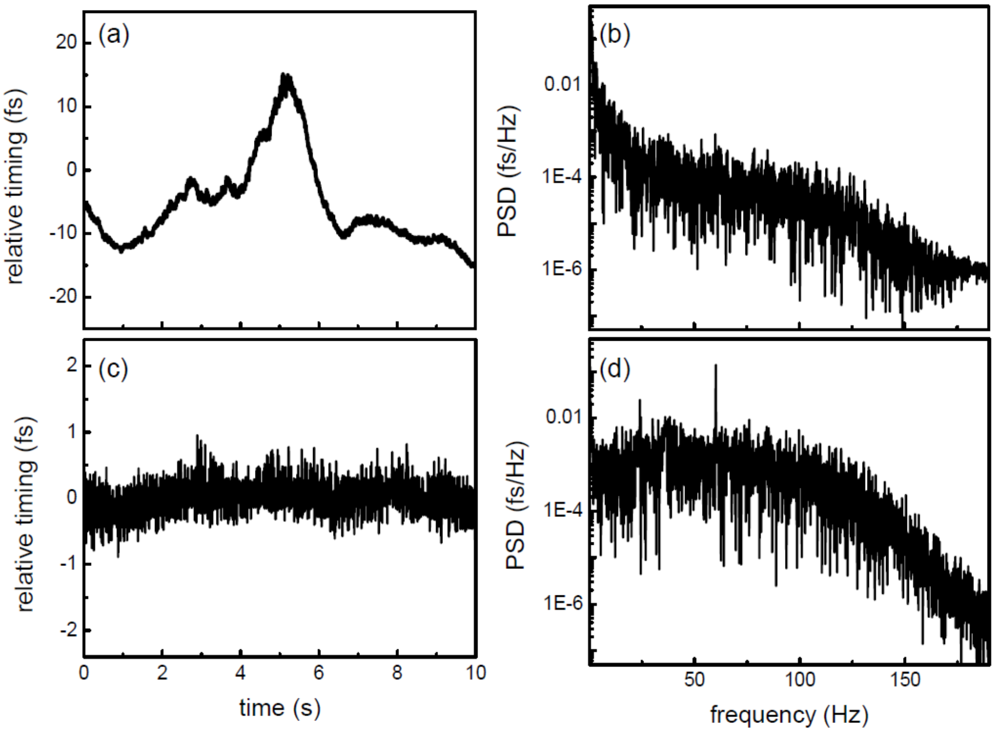

Figure 11. (a) Without the feedback loop, the relative timing experience a drift of 30 fs over 10 seconds. (b) The PSD of the relative timing fluctuation, showing the main noise contribution, is below 30 Hz. (c) With the feeback loop, the r.m.s. relative timing jitter is reduced to 250 as over 10 seconds. (d) The PSD of the residual relative timing jitter. PSD: power spectral density.

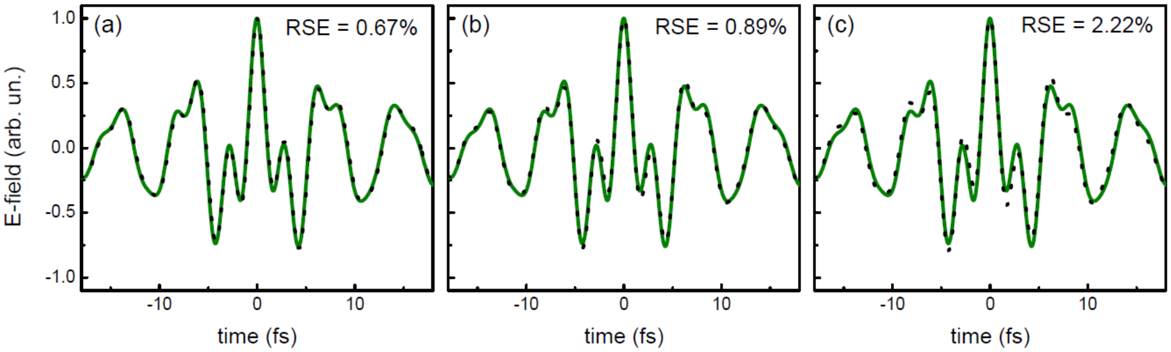

Figure 12. Waveforms under r.m.s. residual jitters. While the green solid line is the unperturbed waveform, the black dotted line is obtained by adding 135 mrad to φ1 in (a), adding 127 mrad to φ2 in (b), and adding 250 as to Δt in (c). RSE: relative squared error.

1.2. Characterization and Shaping of Single-Cycle Pulses

To characterize the synthesized pulse, a two-dimensional spectral-shearing interferometer (2DSI) [9], a variation of spectral-shearing interferometry, is used. In 2DSI, there is no delay between the two spectrally shifted copies of the measured pulse and thus no spectral interference is present. Rather, the group-delay at each wavelength is encoded in the phase of the interference fringes along a wavelength independent axis, created by scanning the relative phase between the two spectrally shifted copies (τ_{gd}). Thus, 2DSI is free from the challenge of calibrating interferometer delay. The two-dimensional intensity plot can be expressed as

$$\begin{aligned} I\left(\omega,\phi_{gd}\right) &= 2\left|A(\omega)\,A(\omega-\Omega)\right|\cos\left\{\phi_{gd}+\left[\phi(\omega)+\phi_{CE}\right]-\left[\phi(\omega-\Omega)+\phi_{CE}\right]\right\}+D.C. \\ &\approx 2\left|A(\omega)\,A(\omega-\Omega)\right|\cos\left[\phi_{gd}+\tau_{gd}\left(\omega-\Omega/2\right)\cdot\Omega\right]+D.C. \end{aligned} \qquad (1)$$

, where $\phi(\omega)$ is the spectral phase, Ω is the shear frequency, ϕ_{CE} is the CEP, and $\tau_{gd}(\omega)$ is the wavelength-dependent group-delay. As shown in equation (1), the spectral phases and the relative timing of the two OPCPA pulses can be determined, but not the CEPs as a constant phase is cancelled in the interference of the two spectrally shifted copies. However, the CEPs can be measured in situ when strong-field experiments are conducted. For example, it has been shown that the actual CEP value can be determined by monitoring of the asymmetry between above-threshold ionization spectra obtained at opposite directions with respect to the laser polarization. In this way, the CEPs (φ1 and φ2) not only can be changed by tuning of any dispersive elements such as the AOPDFs, they can also be determined without ambiguity and with high precision.

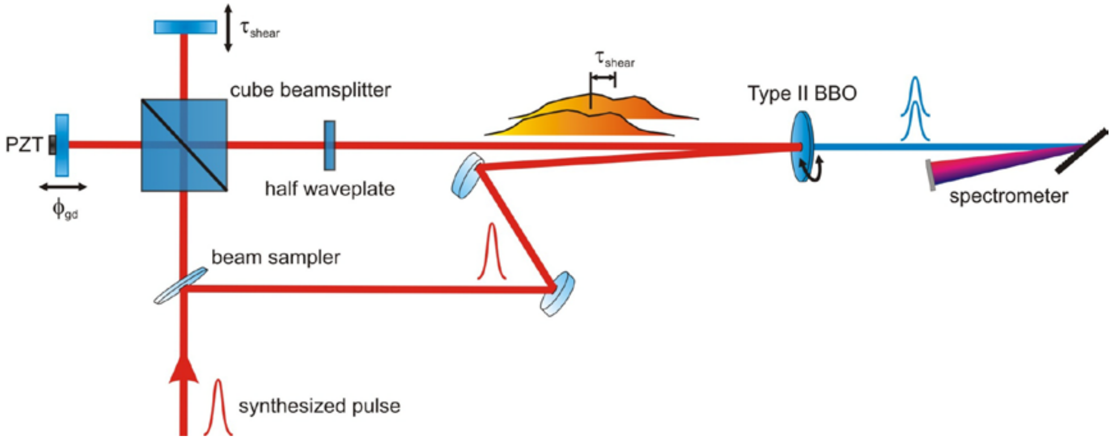

Figure 13. Scheme of the 2DSI for characterizing the synthesized pulse. To observe the interference between the two spectrally shifted up-converted pulses, which encodes the wavelength-dependent group-delay information, the delay of one of the highly chirped pulses is scanned by a PZT-mounted mirror over a few optical cycles. Due to the strong chirp, the scanning of the delay can be approximated as a pure phase modulation (φ_{gd}).

Figure 13 shows the schematics of the 2DSI. The synthesized pulse is first split by a beam sampler whose second surface is anti-reflection coated. A part of the beam (4%) is Fresnel reflected and only guided via silver mirrors before being mixed in a 40-μm type II BBO. The other part of the beam (96%) passes through the beam sampler and is highly stretched before being split again by a cube beamsplitter, routed to the BBO and mixed with the unchirped pulse. The portion mixed with the unchirped pulse is purely derived from the NIR-OPCPA to ensure there is a definite reference for the measured wavelength-dependent group-delay throughout the whole spectrum from 700nm to 2500nm. Two collinear, temporally overlapped, but spectrally sheared upconverted pulses are then generated from the mixing of the unchirped pulse and the two chirped pulses. The shear frequency is set at 14.5THz such that a temporal window over which the pulse can be reliably measured without phase ambiguity is 70fs. To observe the interference between the two upconverted pulses, which encodes the wavelength-dependent group-delay information, the delay of one of the highly chirped pulses is scanned over a few optical cycles. Due to the strong chirp, the scanning of the delay over a few optical cycles can be approximated as a pure phase modulation (τ_{gd}). The spectrum of the upconverted signal is recorded as a function of this delay, yielding a two-dimensional intensity plot that is shown in Figure 14a. The interpretation of the 2DSI data is relatively straight-forward: each spectral component is vertically shifted in proportion to its group-delay.

Figure 14b plots (dashed lines) the wavelength-dependent group-delay of the synthesized pulse extracted from the 2DSI measurement (Figure 14a). It shows that the two OPCPA pulses are temporally overlapped and each is well compressed to within 10% of its transform-limited pulse duration. Figure 14c plots a synthesized electric-field waveform and intensity profile assuming the CEPs (φ_1=650mrad, φ_2=-750mrad) optimal for achieving the shortest high-field transient, which lasts only 0.8 cycles (amplitude FWHM) of the centroid frequency (λc = 1.26 μm). The lower inset of Figure 14c clearly shows that the synthesized electric-field waveform is non-sinusoidal and the main feature lasts less than an optical cycle. Due to the large gap in the combined spectrum, there are wings 4.8 fs from the central peak as shown in Figure 14c. As we will show later, for processes initiated by strong-field ionization, these wings have a negligible effect. For more demanding applications, the wings can be suppressed by extension of the coherent wavelength multiplexing scheme to include a third OPCPA, centered at 1.5 μm, to fill the spectral gap. As an example of waveform shaping made possible by tuning parameters of our system, Fig. 15a and 15b show two atypical waveforms as the CEP and the relative timing are changed.

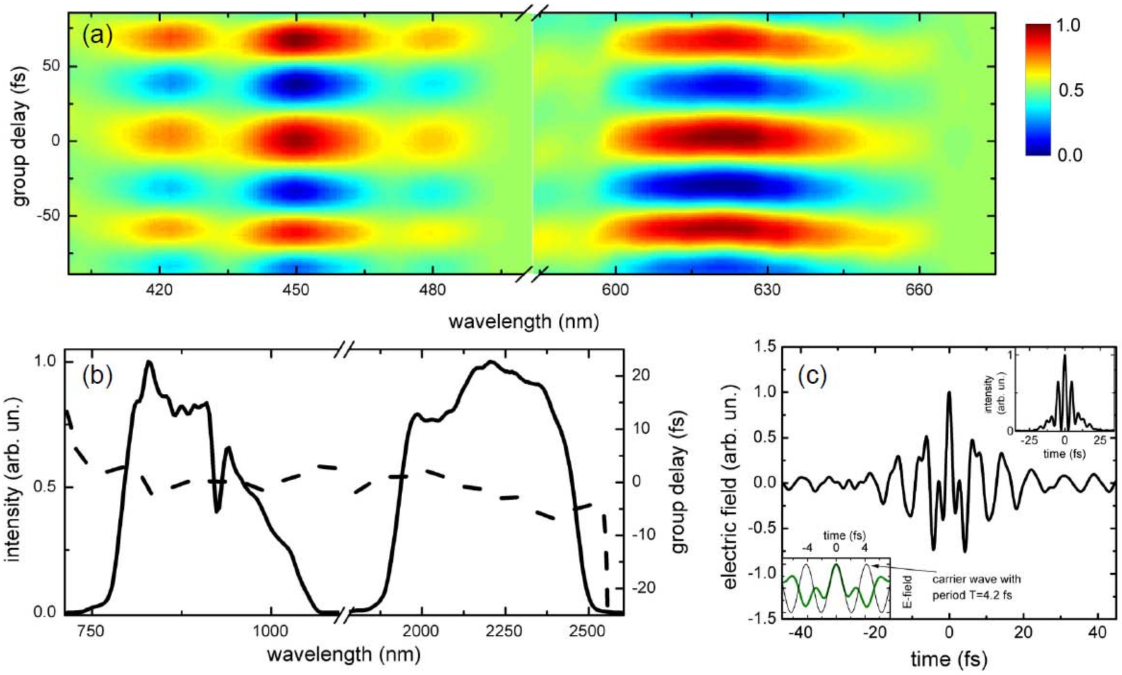

Figure 14. (a) 2DSI data of the synthesized pulse. (b) The extracted wavelength-dependent group-delays superimposed on the OPCPA output spectra. (c) The synthesized electric-field waveform assuming CEPs (φ1=650 mrad, φ2=-750 mrad) optimal for achieving the shortest high-field transient, which lasts only 0.8 cycles (amplitude FWHM) of the centroid frequency. Lower inset: the synthesized waveform is superimposed with the electric field oscillating at the centroid frequency, showing that the synthesized waveform is non-sinusoidal and the main feature lasts less than an optical cycle. Upper inset: corresponding intensity profile.

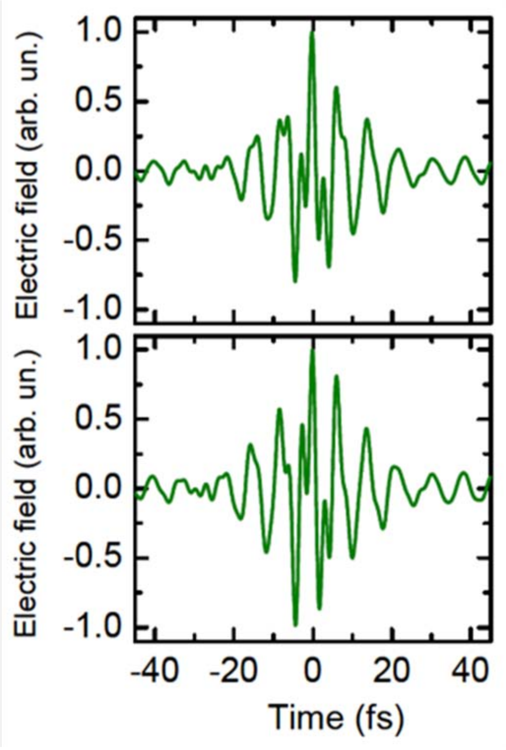

Figure 15. As an example of waveform shaping made possible by tuning parameters of our system, two additional atypical waveforms are shown. (a) A synthesized waveform with φ1=1150 mrad, φ2=-250 mrad, and Δt=0fs. (b) A synthesized waveform with φ1=650 mrad, φ2=-750 mrad, and Δt=1fs.

Beside the temporal shape, the process of HHG is also sensitive to the spatial properties of the driving field. Thus we are extending the capability of the 2DSI to the full spatio-temporal characterization. Due to the collinear nature of the 2DSI measurement, the fringe as shown in Fig. 14 is available at each point in the beam profile. This will result in a 4D data set (a 2D fringe obtained at each transverse spatial coordinate) from which the spectral group delay can be obtained at each point in the beam.

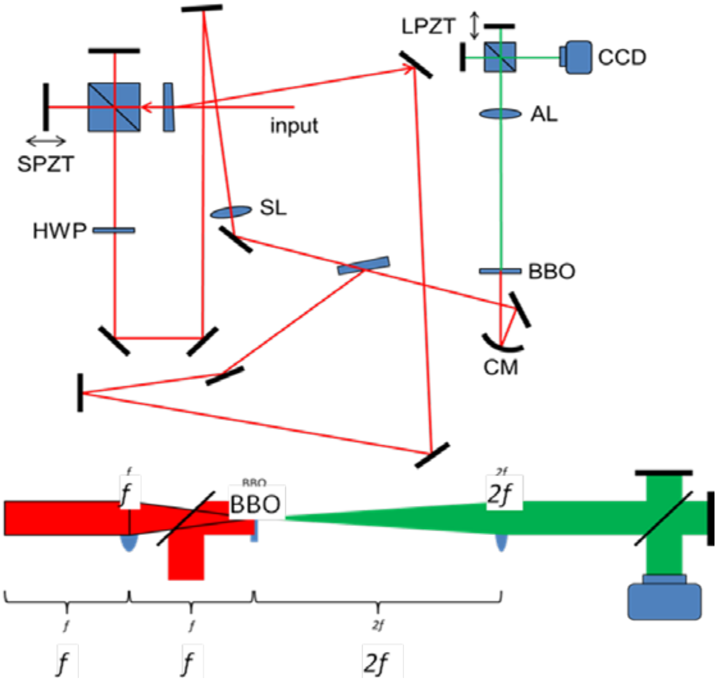

Figure 16. (a) Scheme of the 4DSI for the spatio-temporal pulse characterization. HWP: half waveplate; SL: spherical lens; CM: concave mirror; AL: achromatic lens; SPZT: short-range PZT; LPZT: long-range PZT. (b) Zoom-in view of the different focusing conditions between the two beams and the imaging spectrometer.

Figure 16 shows the schematics of the current 4DSI setup, which shares the basic configuration with the 2DSI. However, while the pulse under test is focused onto the BBO crystal, the chirped pulses are collimated at the BBO crystal. This way, the chirped pulses can not only be treated as monochromatic waves but also be treated as plane waves. A full 2DSI measurement at a 2D array of points along both transverse axes can be done using an imaging spectrometer. To obtain sufficient spectral resolution, 1600 image frames has to be taken for the spectrum reconstruction. If a continuous phase modulation (as done in 2DSI) is performed, the total image frames to be taken will be more than 200,000. Instead, here we implement the Hariharan phase stepping technique which only requires 5 discrete phase modulations (with a step size of π/2) and the total image frames to be taken is reduced to 8,000. Hariharan algorithm is used for its robustness to phase step calibration errors. The phase reconstruction error introduced by the 10-nm repeatability of our PZT is calculated to be less than 1% (20mrad).

Figure 17 shows the measured spectra and retrieved phases at three different points in the beam profile. The laser under test is a Kerr-lens modelocked Ti:sapphire oscillator which has a spectrum spanning from 700nm to 900nm. The first two spectra resemble each other while the third spectrum is different from the others in the long wavelength part. The retrieved phases follow the same trend as expected since there is a correlation between spectrum and phase in a Kerr-lens modelocked laser. To fully enable the complete spatio-temporal characterization of the pulse, an additional spatial shear interferometer is being built to measure the wavelength dependent spatial phase. Such an apparatus has been demonstrated previously to extend the capability of the SPIDER to the full spatio-temporal characterization [10].

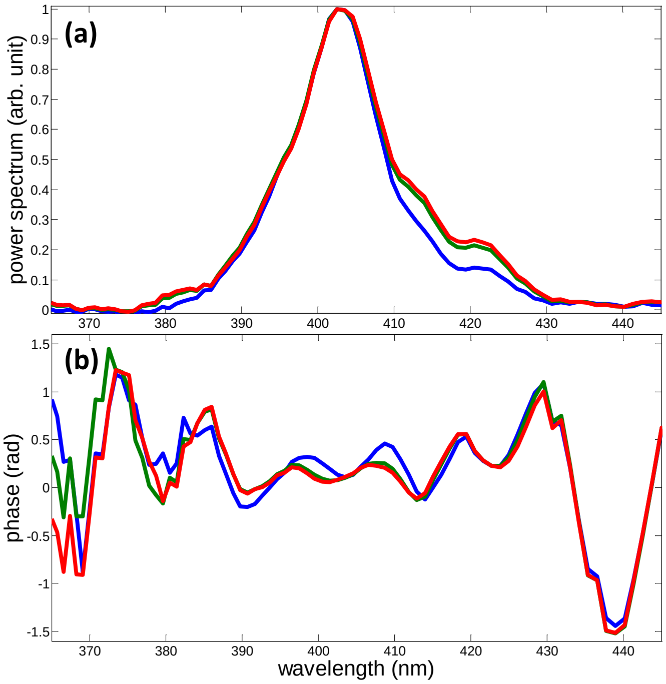

Figure 17. Spectra (a) and reconstructed phase (b) measured at three different transverse points of the beam.

2. Theory of HHG and attosecond pulse generation driven by synthesized sub-cycle waveforms

Prior to our work on coherent wavelength multiplexing (Section 1), isolated sub-cycle waveforms with a pulse-energy sufficient for optical field ionization were not available for driving attosecond pulse generation. Accordingly, there has been little prior theoretical work on the effects of such pulses on high harmonic generation (HHG) and attosecond pulse generation processes. Supporting the objectives of Years II and III of our AFOSR program, we have completed several theoretical studies with the aim of making clear how these unique waveforms might be used to optimize attosecond pulse sources. In section 2.1, our study has elucidated new opportunities for control of isolated attosecond burst properties inherent to HHG driven by sub-cycle waves. In section 2.2, we show how the synthesized waveforms generated via our coherent wavelength multiplexer can be used to generate isolated soft-X-ray attosecond pulses without the use of temporal gating techniques.

2.1. Carrier-envelope phase dependence of HHG with sub-cycle waveforms

The coherent synthesis of multi-color broadband spectra, as described in Section 1, has enabled the generation of phase controlled sub-cycle pulses [11,12]. The capability of optimizing the shape of the electric-field waveform of non-sinusoidal pulses, through modification of its carrier and envelope, most notably the carrier-envelope phase (CEP) relationship, enables control of strong field laser-atom interaction for XUV spectroscopy and attosecond pulse generation. Although HHG from few-cycle to sub-two-cycle pulses as well as periodic trains of non-sinusoidal pulses has been amply explored [3,13-15], the case of sub-cycle pulses has so far received limited attention. Here we report and compare calculations for HHG driven by sub-cycle and 1.5-cycle pulses that illuminate extreme carrier-envelope phase (CEP) sensitivity of cut-off energy and provide enhanced control for generation of attosecond pulses.

It has been theoretically shown that the electron recollision energy can by controlled by shaping the electric field waveform within an oscillation period [15]. As the FWHM driver pulse approaches the sub-cycle regime, the electric field envelope varies rapidly from one half cycle to another and thereby facilitates strong CEP dependence within a single optical cycle. Fingerprints of CEP dependence such as frequency shifting of the harmonics close to cut-off and change in the shape of the cut-off itself have been observed only for few cycle pulses. As we move towards sub-cycle pulses (for example, 2–3 fs @ 800nm), the CEP effects are more dramatic. We have identified and explored two of these effects: a change in cut-off shape and energy and the implementation of *intra-cycle* ground state depletion gating for isolated attosecond pulse generation. The discussion is based on the single atom response using the Three Step Model in the single active electron approximation [16]. To keep the dynamics simple, we used a Gaussian shaped pulse ensuring that there is no dc component.

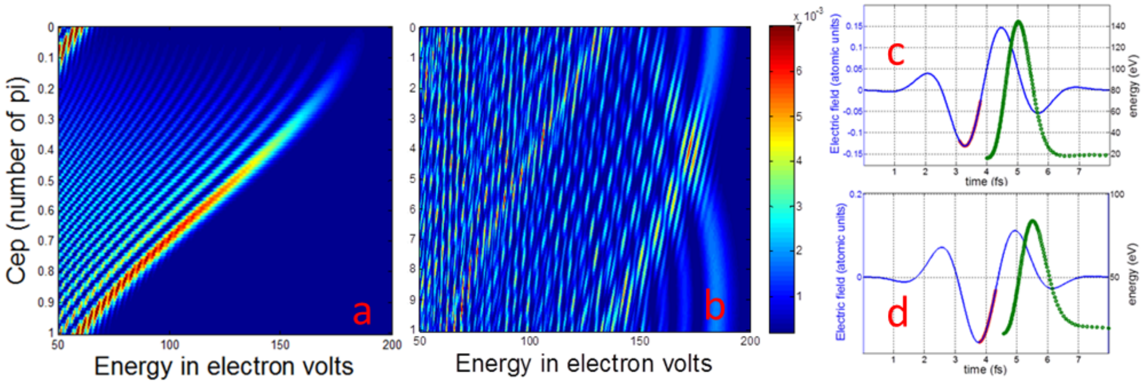

Figure 17. CEP dependent harmonic spectrum at 800 nm for a laser pulse of duration (a) 2 fs pulse and (b) 4 fs pulse at a peak electric field corresponding to $I = 8 \times 10^{14}$ W/cm^2. (c) and (d) show the electric field waveform (blue) and the kinetic energy versus time plots of the trajectories (green) for CEP of 0.4π and 0.8π, respectively. The electric field corresponding to the birth of the trajectories is marked in red.

The CEP dependent harmonic spectrum of Ar for a 2 fs (Fig. 17a) and a 4 fs (Fig. 17b) driver pulse at 800 nm and a peak intensity of 8.9 x 10^{14} W/cm^2 are shown. For the 4 fs pulse, the cut-off is made up of discrete harmonics for only a small range of CEP values 0.2π to 0.5π. For other CEP values a smooth continuum is observed at the cut-off, indicating an isolated attosecond pulse when properly filtered. The cut-off is a continuum when the CEP dependent electric field waveform creates the most energetic photons in a single optical half-cycle. For the 2-fs pulse, a broad continuum at the cut-off is always observed. Additionally, the energy of the cut-off drops sharply by about 100 eV as we sweep the CEP form 0.2π to π. In this case, one can uniquely infer the CEP of a sub-cycle pulse by looking at the cut-off of the harmonic spectrum. This is qualitatively different from the method employed in [13], where the shape of the cut-off was used to determine the CEP. Since there is only a single ionization event, harmonics are not observed, rather we see an interference pattern between the long and short quantum trajectories. Fig. 17c and Fig. 17d show the electric field waveforms of the 2fs sub-cycle pulse for a CEP value of 0.4π and 0.8π, respectively. The green curve shows the energy versus time plot of the returning trajectories and the electric field values where they are born is highlighted in red. When the CEP value changes from 0.4π to 0.8π, the electric field following the ionization event gets suppressed and therefore the electron trajectories return back with lower kinetic energy resulting in a red-shifted HHG spectrum.

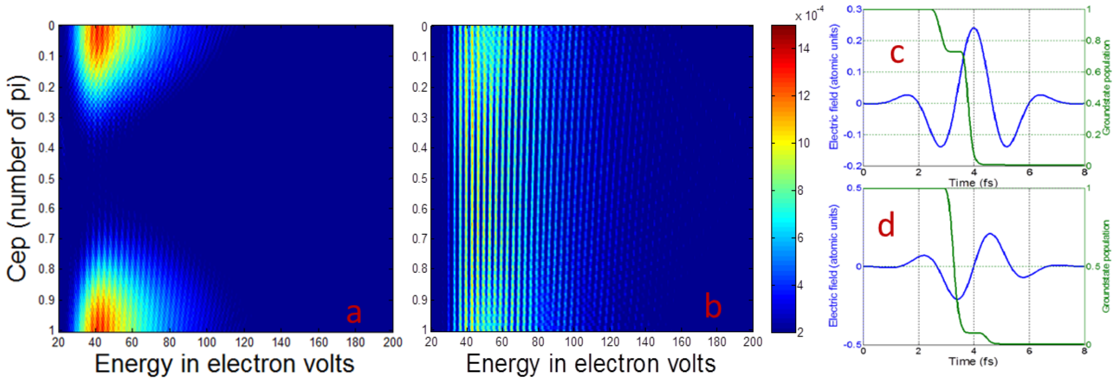

Figure 18. CEP-dependent harmonic spectrum at 800 nm for a laser pulse whose duration is (a) 2 fs pulse and (b) 4 fs pulse for a peak electric field corresponding to 2 x 10^{15} W/cm^2. In (c) and (d) the 2 fs electric field waveform (blue) and ground state population (green) for CEP values of 0 and 0.5π, respectively.

The aforementioned behavior of the cut-off changes dramatically once again when the electric field becomes strong enough to deplete the ground state (Fig. 18). For the sub-cycle pulse of peak intensity 2×10^{15} W/cm^2 and zero CEP (Fig. 18a) a smooth continuum centered at 45 eV is observed while at 0.5π CEP, harmonic radiation is suppressed due to ground state depletion (Fig. 18d). For the 4-fs pulse (Fig. 18b), the harmonics between 40 eV and 80 eV show only a weak CEP dependence. A drop in cut-off energy for both cases is due to ground state depletion before the most energetic electrons return to the atom. For the sub-cycle pulse (Fig. 18a), there is an additional effect: interference between short and long trajectories within a single half cycle has disappeared because the ground state is completely depleted by the time the long trajectories return. Importantly, this *intra-cycle* ground state depletion allows for shaping of the isolated attosecond burst spectrum and temporal duration. Whereas in the 2-cycle case, ground state depletion has been used to generate isolated attosecond pulses [17] where depending on CEP one or two attosecond bursts of XUV photons are generated, with sub-cycle pulses, isolation of a single pulse takes place uniformly, and the CEP can be used to control attosecond pulse properties. Most notably, pulse emission is completely suppressed for CEP around 0.5π.

In conclusion, sub-cycle pulses provide tremendous control of high harmonic generation processes, with effects not possible with even 1.5 cycle pulses. These basic effects of sub-cycle waveform driven HHG, including the amplitude and phase shaping of attosecond pulses through the modification of the CEP, will be explored in experimental work conducted in the future.

2.2. Isolated soft X-ray pulses generated by waveforms synthesized from 800-nm and 2-μm OPCPAs

To predict the properties of the attosecond bursts that can be generated by the novel multiplexed 800-nm and 2-μm OPCPA pulses described in Section A, we have performed numerical time-dependent Schrödinger equation (TDSE) simulations of HHG driven by them. These simulations confirm the anticipated advantage of using sub-cycle waveforms for isolated attosecond pulse generation. Due to the inherent half-cycle symmetry of the HHG process, attosecond bursts are emitted with each half-cycle peak of a multi-cycle pulse. Thus, techniques such as polarization gating [18,19], two-color gating [20,21], ionization gating [22], double optical gating [23], and ground-state depletion gating [17] have been used to produce isolated attosecond pulses when the driving pulse duration is more than an optical cycle. These techniques open up the field of attosecond science, but the efficiency is fundamentally limited because energy outside the gating period is not used. Single-cycle and sub-cycle driving pulses can be used for generating the shortest and most intense isolated attosecond pulses with a given driving pulse energy. Moreover, by shaping the driving pulse [24] and altering its CEP (Section 2.1), one can control the spectral phase of the harmonics, allowing more control for compressing the attosecond pulses.

As an example, we numerically solved the TDSE for a He-atom in a laser field corresponding to our multiplexed 800-nm/2.15-µm pulse source (Section 2.1) to illustrate a possible use of our source for driving direct isolated soft-x-ray pulse generation (Figure 18). The peak intensity of 6×10^{14} W/cm^2, which can be reached with a beam diameter of 27 μm, was chosen such that the total ionization is below the critical ionization level in helium. The transmission and dispersion of the Sn filter were taken from reference [25]. Details about the TDSE solver are described in reference [11]. To gain more insight into the results given by the 3D TDSE simulation, we also calculated the ionization dynamics using the ADK formula (the blue curve in Figure 18a) and the classical electron trajectories (overlaid on top of the spectrogram in Figure 18b). Electron trajectories from three ionization events, which are labeled by numbers, were calculated and those trajectories that return to the ionized atom are shown in Figure 18b. For visualization, electrons ionized by the electric field with strength weaker than half of the maximum were neglected since they have negligible contribution to the HHG emission, as confirmed by the TDSE simulation.

With choice of CEPs as in Figure 18a, substantial ionization is limited to one optical half-cycle and an isolated soft-x-ray pulse spanning over 250 eV is generated (Figure 18b and 18c) without the need for gating techniques or spectral filtering which typically limit the efficiency and the obtainable bandwidth. Using an additional Sn filter, which blocks the strong IR driving field and the nonlinearly chirped low-photon-energy spectral content below 70 eV, leads to an isolated 150-as pulse centered at 200 eV. Of note, the non-sinusoidal electric-field waveform leads to drastically changed electron trajectories (compared to those from a sinusoidal driving field) resulting in corresponding changes in quantum diffusion and atto-chirp, which can be controlled by means of the waveform synthesis parameters (φ_1, φ_2, and Δt, see Section 1).

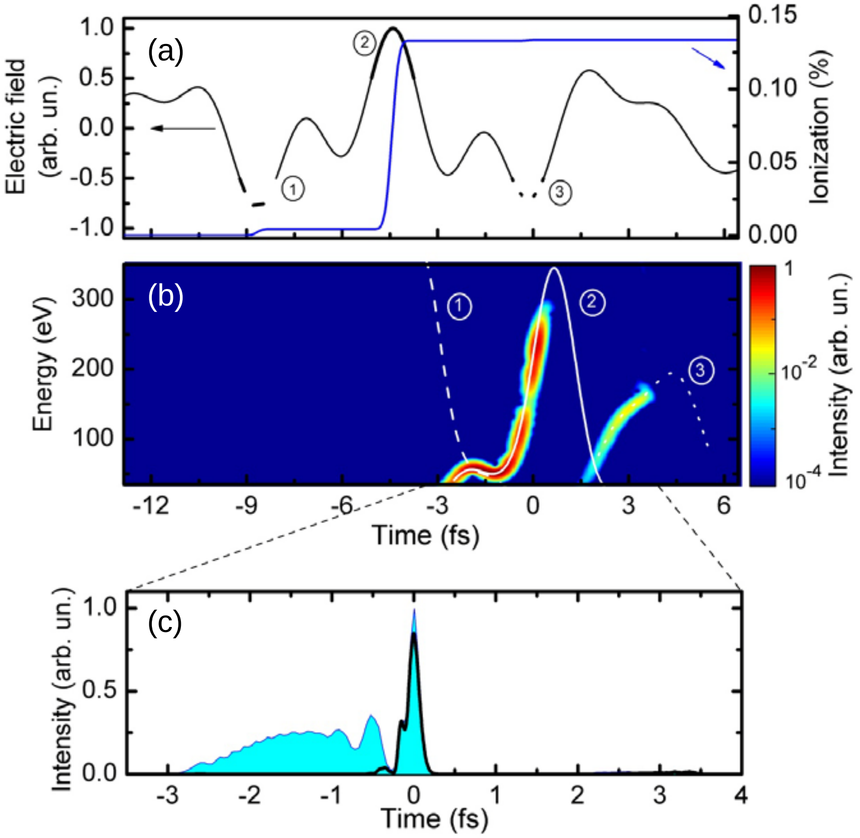

Figure 18. TDSE simulation results of the single-atom HHG with the synthesized waveforms. (a) Ionization dynamics (blue) induced in helium by a linearly polarized electric-field waveform (black) assuming a peak intensity of $6\text{x}10^{14}$ W/cm^2, φ_1=960 mrad, and φ_2=-440 mrad. (b) Spectrogram of the HHG superimposed with the calculated classical trajectories. Returning trajectories from three ionization events (2: the main pulse; 1 and 3: the satellite pulses) are shown for clear interpretation of the spectrogram. The synthesized pulse isolates the ionization process to a half optical cycle and a continuum spectrum spanning more than 250 eV can be achieved. The isolated soft x-ray pulse has the same sign of chirp over 80% of the spectrum and so the compression setup can be simplified. (c) The isolated soft x-ray pulse plotted in the time domain before (blue) and after (black line) a 100-nm thick Sn filter. The Sn filter is chosen for its capability to block the strong IR driving field and the nonlinearly chirped low-photon energy spectral content, and its good transmission in the soft x-ray range. The filtered isolated soft x-ray pulse has a FWHM duration of 150 as.

In HHG, quantum diffusion and ionization rate are two competing factors in determining the ratio between radiation from long and short electron trajectories. While quantum diffusion always favors the short trajectories, when the HHG process is driven by conventional sinusoidal electric-field waveforms, the stronger ionization rate for the long trajectories results in significant radiation from electrons of both trajectories. For the example shown in Figure 18b, where a sub-cycle waveform is used, the difference in travel time between long and short trajectories is increased. In addition, the ionization contribution to short trajectory radiation is boosted. Overall, quantum diffusion dominates over ionization rate and effectively eliminates the radiation from long trajectories, resulting in isolated soft x-ray pulse generation solely from short trajectories. This gives an example of the capability of our light source to simultaneously isolate the ionization process and manipulate electron trajectories within an optical cycle, allowing unprecedented control of the HHG process.

3. HHG and attosecond pulse generation experiments (Years 2/3 objectives)

3.1 FROG-CRAB setup and results with a CPA Ti:sapphire laser

We have developed an actively stabilized attosecond streaking interferometer for frequency resolved optical gating for the complete reconstruction of attosecond bursts (FROG-CRAB) [26], as illustrated by Fig. 19. All components of the interferometer were carefully designed to ensure that they can work reliably with the various drive sources developed in our group, ensuring a reliable working range from 800 nm to beyond 2.15 μm. To do this, a custom broadband gold beamsplitter, fabricated at MIT, is used to split the drive and streaking path of the experiment. The splitting power ratio is readily customizable to any desired value depending on the specified gold thickness. For HHG of EUV pulses, one path of the incoming drive laser is focused onto a high frequency pulsed gas-jet tuned to the repetition rate of the laser (currently 1kHz). From here, the long wavelength driver light is filtered out using a thin metalic film (usually Al), which also acts to remove the inherent chirp of the generated XUV pulses. The transmitted EUV light is then focused using a gold plated toroidal mirror at 86° grazing incidence into the focal region of an electron time of flight (TOF) spectrometer. It is in this region that the sample of interest, for example a freely expanding gas or solid target, is located

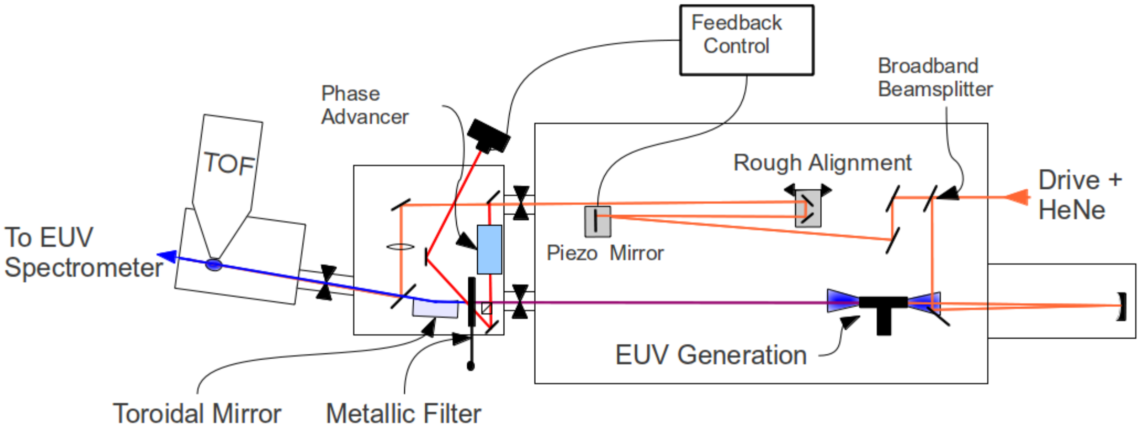

Figure 19. Schematic of completed FROG-CRAB apparatus. The custom broadband beamsplitter can support drive beams from 800 nm to beyond 2 μm. A cw HeNe beam runs along a majority of the path length of the streak and drive beams until being picked off in the second chamber, where it is phase delayed and enters an interferometer. Locking this loop adds stability as well as a fine control mechanism for adjusting overal streak path delay. The long wavelength drive source is separated from the XUV using metalic filters, and the XUV beam is then focused at the opening of a time of flight spectrometer (TOF), using a toroidal mirror. The toroidal mirror is aligned to image the source, with XUV spot sizes less than 40 μm. The outer portion of the streak beam is focused onto the same spot for energy modulation of photoelectron spectra.

The transmitted pulse, referred to as the streaking pulse, is meanwhile delayed using a piezo controlled stage before being loosely focused and recombined with the generated XUV pulse using a drilled mirror. The drilled mirror allows full transmission of the XUV pulse, while picking off an annular portion of the streaking pulse. The delay timing is measured and stabilized using a HeNe based interferometric feedback loop that is superimposed on a majority of the beampath taken by the drive and streak beams. Using polarization optics, the phase of one arm of the HeNe interferometer can be adjusted continuously in one direction with a precision down to 7 µrad, giving the delay a theoretical resolution of $7\text{x}10^{-4}$nm when the interferometer is locked. With the feedback loop active, timing jitter less than 250-as r.m.s. has been obtained.

This system has already been used to streak attosecond pulse trains using 35 fs drive pulses at 800 nm from our commercial Ti:Sapphire regenerative amplifier. Our most recent results clearly demonstrate streaking of the attosecond photoelectron pulse train. In Fig. 20, two experimental photoelectron spectra are shown. The one on the left was taken without the streak beam present, and the one on the right with the streak beam present. Due to the streaking beam's presence, the photoelectron pulse train is no longer anti-symmetric over one half cycle of the laser as electrons in one half-cycle are “pushed” while those in the next are “pulled” by the strong laser field (see Fig. 21 (a)). This symmetry breaking leads to the appearance of even harmonic components [27] as seen in Fig. 20 (b).

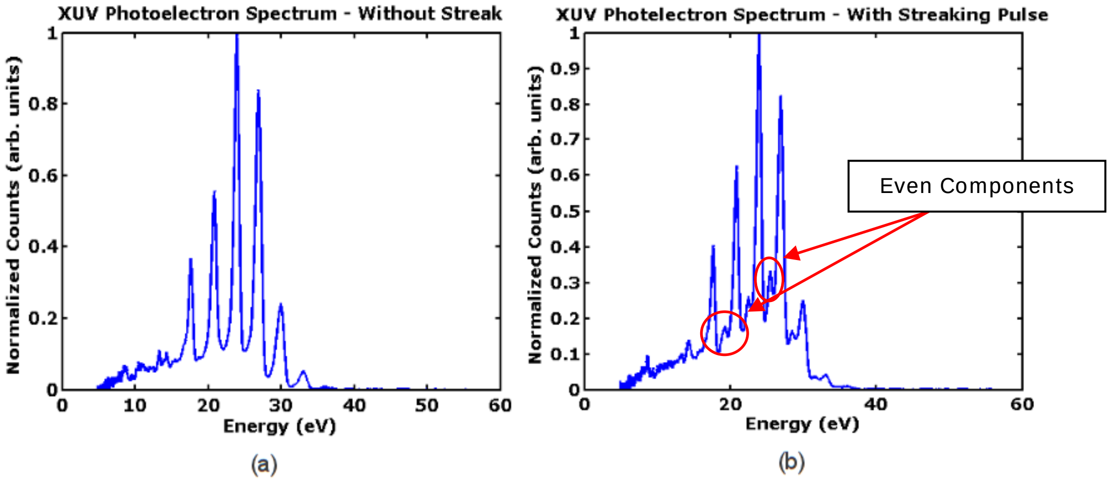

Figure 20. Demonstration of photoelectron spectra (a) without and (b) with streak beam present. In (b) the presence of even components is due to breaking of antisymmetry between consecutive attosecond pulses.

Furthermore, we have also measured a full streaking trace of the XUV pulses which matches qualitatively well with simulations having similar experimental parameters. Fig. 21 shows the simulated XUV pulse train with IR streak superimposed, along with the simulated and experimental trace. The individual XUV pulses were modeled as

$$E_{xuv} = E_n \exp\left\{-2\log(2)t^2(1+i\xi)/[\tau^2(1+\xi^2)]\right\},$$

where τ is 200 as, and ξ is used to simulate the inherent chirp on the XUV pulse, here set to be sqrt(3), and n is the pulse number. Depending on the relative positioning of the IR streaking beam to the XUV pulse train, more or less energy is coupled into the even spectral components. Simulations show that at our current streak energies, we are not able to clearly deconstruct the FROG-CRAB spectrogram to measure the attosecond pulse form. Subsequent measurements with higher streak energies are forthcoming.

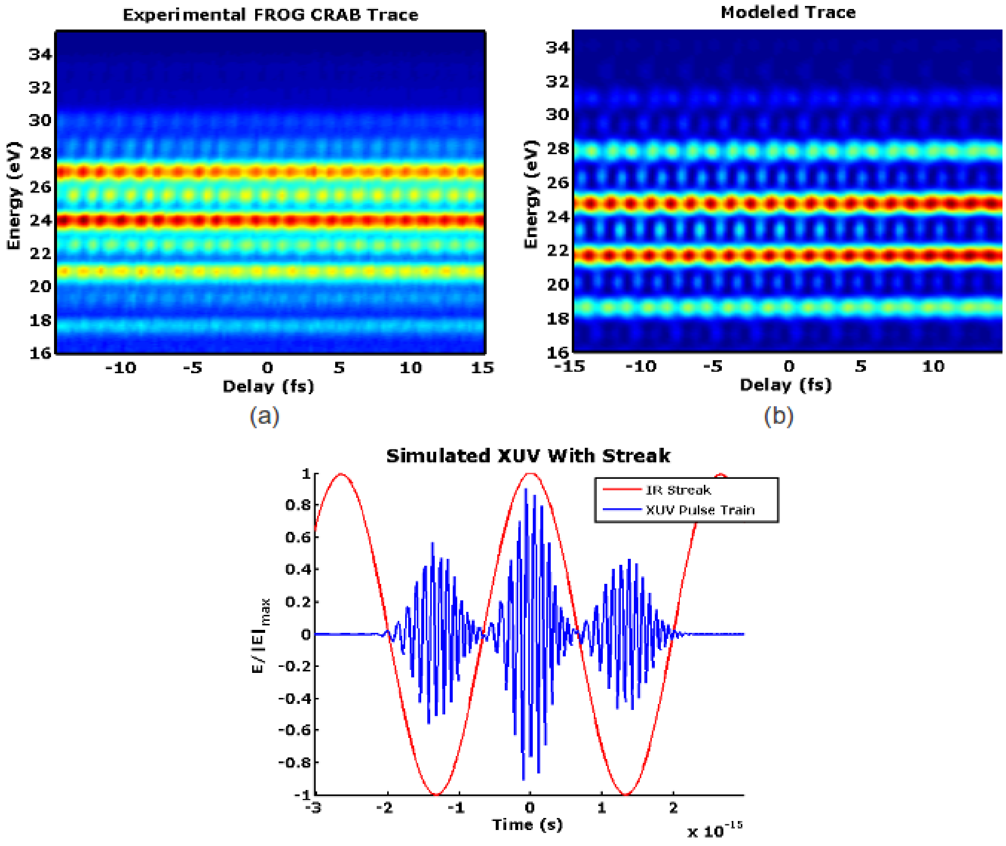

(a) (b)

(c)

Figure 21. In (a) we show our first experimental FROG-CRAB trace, clearly showing a modulation of the spectra with respect to the streak delay position as the energy is transfered from odd to even and then back to odd energy components. (b) Simulated FROG-CRAB spectrum for 200 attosecond transform limited XUV pulses with a 35 fs, 800 nm streak beam having peak intensity of roughly 1×10^{11} W/cm^2, closely matching the experimental conditions. (c) Demonstration of the normalized XUV pulses used for simulation within the 800 nm streaking beam. Electron bunches made within the central peak of the vector potential are “pushed” while those in the valleys are “pulled” breaking the anti-symmetry of the original pulse form and maximizing the even spectral components. When the pulses are located at the nodes, of the vector potential, only a small perturbation is applied thus minimizing the even spectral components.

3.2 Upgrade of OPCPAs using a cryogenically-cooled Yb:YAG pump laser

Energy scaling of the sub-cycle pulse synthesizer described in section 1 is possible with the novel pump laser technology based on the cryogenic picosecond Yb-doped laser amplifier we have developed over last years. In this section, we first describe the upgrade of the 2-μm, kHz, OPCPA in the pulse synthesizer to a mJ-level source using a cryogenic Yb:YAG pump laser and its application to the long-wavelength-driven HHG towards water-window soft-X-ray radiation. Second, we present the progress of the energy upgrade of 800-nm OPCPA. Because of the excessive energy of 13 mJ from the cryogenic Yb:YAG CPA laser, the synthesized pulse energy from two OPCPAs can be boosted up to mJ level, which enables to achieve the isolated attosecond pulse generation and phase-sensitive control of HHG process, as described in the theory section.

3.2.a) High-energy, phase-stable, kHz OPCPA at 2.1 μm pumped by a ps cryogenic Yb:YAG laser and its application to HHG

The 2-μm OPCPA in the pulse synthesizer itself is a very useful source for attosecond science because long-wavelength driven HHG [28-33] is a promising way of high-flux coherent extreme ultraviolet/soft X-ray (XUV) radiation with photon energies approaching the keV regime via cutoff extension. However, the single-atom response in the HHG efficiency unfavorably scales with driving wavelength (λ^{-5} for the cutoff region and λ^{-6} for the plateau region), which makes phase matched and absorption limited generation important for practical use, in order to avoid an additional efficiency drop. In general, mJ-level pulse energy is necessary to avoid the phase mismatch induced by the Guoy phase shift, as demonstrated using a 10-Hz, 2.4-mJ, 2-μm optical parametric amplifier (OPA) pumped by a Ti:sapphire chirped-pulse amplification (CPA) laser [33]. The generated XUV photon number per second over 1% bandwidth, however, is still as low as $\sim 6 \times 10^7$, limiting potential applications. Increasing the repetition rate to the kHz-range is a clear path towards increasing XUV photon flux by 2 orders of magnitude. More recently, sub-mJ few-cycle kHz OPA sources at around 1.8 μm, pumped by a kHz CPA Ti:sapphire laser, have been demonstrated with the help of external pulse compression techniques [34,35].

OPCPA is generally regarded as a more energy-scalable method than OPA, but the generation of >mJ energy from OPCPA at kHz repetition rates is nontrivial due to the lack of suitable pump sources. Since the energy scaling of such OPCPA systems at kHz repetition rate is ultimately limited by the power and energy handling of Nd:YLF laser technology, new pump laser technologies based on Yb-doped laser materials are now being rapidly developed. Cryogenically-cooled Yb-doped laser technology provides a straightforward way of energy and average power scaling [36-39]. Recently, we have demonstrated 40 mJ amplification of ps pulses at 2 kHz from a cryogenic Yb:YAG CPA chain [40]. Compared to the thin-disk regenerative amplifier (RGA) [41], the cryogenic Yb:YAG RGA has the distinctive advantage of using a much lower number of roundtrips (<15 vs. ~150) thanks to the higher single-pass gain, which is crucial for stable operation of RGAs without bifurcation and reliable optical timing synchronization with the OPCPA seed pulses.

In this subsection, the energy scaling of a 2.1-μm kHz ultrabroadband OPCPA system is achieved using a high-energy, ps cryogenic Yb:YAG pump laser [40], optically synchronized to the signal. We demonstrate 2.1-μm driven HHG results with Xe, Kr, and Ar gases.

A. Pump lasers and optical synchronization

The ultrabroadband 2.1-μm OPCPA system operating at 1 kHz repetition rate consists of a master oscillator with a DFG stage, a Nd:YLF pump laser, a cryogenic Yb:YAG pump laser, and three OPCPA stages followed by a compressor. Figure 22 shows the optical synchronization scheme of the OPCPA stages with two pump lasers and the CPA schematic of each pump laser. As described in the sub-cycle pulse synthesizer in the section 1, the octave-spanning Ti:sapphire oscillator at 85 MHz generates passively CEP-stabilized seed pulses at 2.1 μm by intra-pulse DFG in a 2-mm-long MgO-doped periodically poled congruent lithium niobate (MgO:PPLN). The 650 nm and 940 nm portions of the Ti:sapphire spectrum are mixed together to generate ultrabroadband spectra around 2.1 μm. The 1-μm portion (1010-1060 nm) of the oscillator spectrum with an average power of ~3 mW is amplified by an ytterbium-doped fiber amplifier (YDFA) to ~20 mW for seeding two pump lasers unlike the original scheme in section 1.

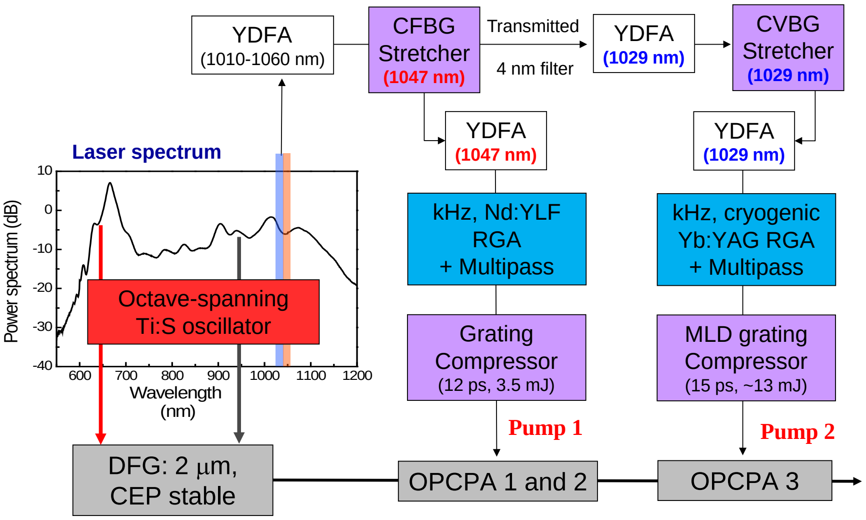

Figure 22. Schematic diagram of a kHz 2.1-μm ultrabroadband OPCPA pumped by Nd:YLF and cryogenic Yb:YAG CPA lasers, optically synchronized to the OPCPA signal. (YDFA, ytterbium-doped fiber amplifier; CFBG/CVBG, chirped fiber/volume Bragg grating; MLD, multi-layer dielectric; RGA, regenerative amplifier)

The first pump source is a 4-mJ, 12-ps, Nd:YLF CPA chain, composed of a chirped fiber Bragg grating (CFBG) stretcher, YDFA, RGA followed by two multi-pass slab amplifiers, and a diffraction grating compressor [42]. This laser pumps the first and second OPCPA stages (pump 1 in Fig. 22). We maintained the energy at ~3.5 mJ after the multipass amplification and compression, which was split into the first and second OPCPA stages with an appropriate ratio using a variable beam splitter while the unused energy was dumped.

The second pump source is a high-energy, 14 ps, cryogenic Yb:YAG CPA chain, which was slightly modified from the original setup seeded by a Yb-doped fiber oscillator [40]. The stretcher is composed of a chirped volume Bragg grating (CVBG) pair with a chirp rate of ~100 ps/nm per bounce. After 8 bounces off the CVBGs, we obtained ~560 ps positively chirped pulses with 0.7 nm bandwidth at 1029 nm. Two YDFAs before and after the CVBG stretcher ensure high enough pulse energy (~100 pJ) for seeding of the cryogenic Yb:YAG RGA. We limited the maximum energy from the two amplifiers to 20 mJ at 1 kHz for damage-free long-term operation. The pulse is compressed using a multi-layer dielectric (MLD) grating pair, where the gratings have a groove density of 1752 lines/mm and a diffraction efficiency of 95%. A throughput efficiency of 75% was achieved and a compressed pulse duration of 14.2 ps was measured using a picosecond autocorrelator. The final energy at the third OPCPA stage is 13 mJ after all optics for pump beam delivery. The use of a single mode-locked Ti:sapphire master oscillator proving all optical seed pulses ensures the timing synchronization between pump and signal pulses at all OPCPA stages.

B. OPCPA setup and amplification result

The 2.1-μm seed pulses with ~2 pJ at 85 MHz and a spectral bandwidth of ~500 nm at -10 dB, generated by intra-pulse DFG in MgO:PPLN, are stretched to ~5 ps with a 30-mm-long silicon block and then amplified to 2.5 μJ at 1 kHz in the first OPCPA stage (OPA1 in Fig. 23) based on a 2-mm-long MgO:PPLN which is pumped by 0.5 mJ of energy from the Nd:YLF laser. The pulses are then stretched to ~9 ps full width at half maximum (FWHM) using an acousto-optic programmable dispersive filter (AOPDF; Dazzler, Fastlite) which also compensates for the high-order dispersion terms to achieve high-quality pulse compression. The second OPCPA stage based on a 2-mm-long MgO:PPSLT crystal, pumped by ~1.4 mJ of energy, amplifies the 2.1 μm pulses to 25 μJ with a spectral bandwidth of 405 nm in full width at half maximum (FWHM) as shown in Fig. 24(a). The pulses are further stretched to ~14 ps (FWHM) in the second 30-mm-long silicon block with a Fresnel reflection loss of ~50% for better matching to the pump pulse duration of the cryogenic Yb:YAG laser at the third stage.

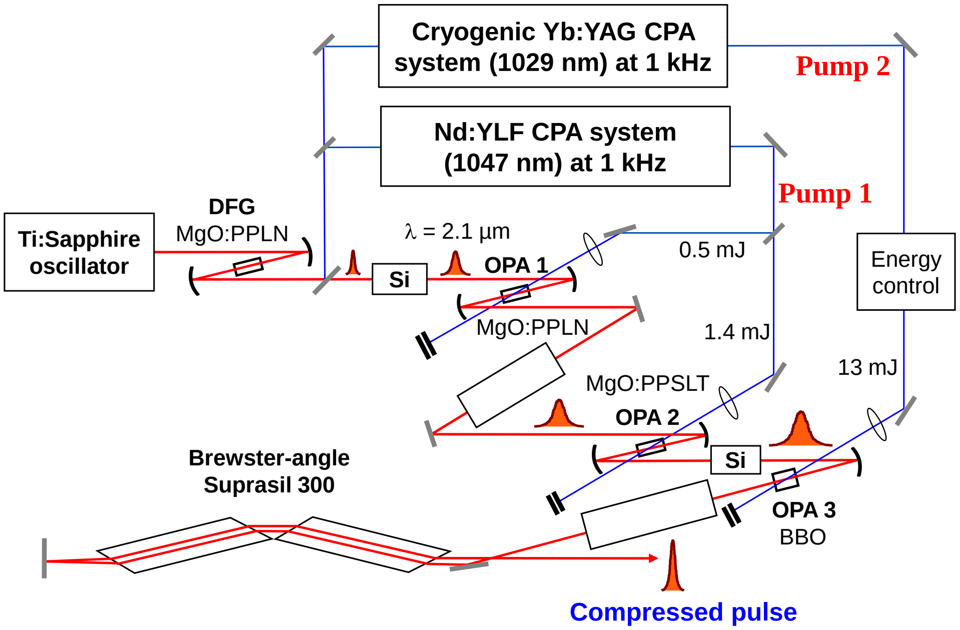

Figure 23. Optical layout of the ultrabroadband CEP-stable 2.1-μm 3-stage OPCPA system. Fine dispersion control is used for efficient amplification with low SF noise. Pulse durations are ~5 ps before the first stage, ~9 ps before the second stage, ~14 ps before the third stage, and 32 fs after the compressor.

Aiming for multi-mJ amplification in the third OPCPA stage, we used a 5-mm-long type-I β-barium borate (BBO) crystal ($\theta=21.4^{o}$). The third OPCPA stage was optimized by varying the pump and signal beam sizes at the BBO crystal while monitoring the output energy and the relative SF noise. At the end, the pump beam size was set to be ~1.4 mm in FWHM while the seed beam size was set to ~4.0 mm in FWHM, which was much larger than the pump beam size for efficient SF suppression and for transfer of the high-quality pump beam mode to the signal beam. The corresponding pump intensity was ~40 GW/cm^2 at 13 mJ of energy. The angle between the pump and the seed was minimized to <2^o to maximize phase matching bandwidth. After optimization of temporal and spatial overlaps and incidence angle of the pump beam into the BBO crystal, we obtained a maximum energy of 0.85 mJ with a pump energy of 13 mJ, indicating a conversion efficiency of 6.5%. The amplified spectrum from the third OPCPA stage is represented as the solid line in Fig. 24(a). The spectral bandwidth of 474 nm FWHM centered at 2.1 μm supports a transform-limited pulse duration of 24.5 fs or 3.5 optical cycles, as shown in Fig. 24(b). An output bandwidth broader than that of the input pulse coming from the second stage (405 nm) indicates gain saturation at the third stage. The pulse compression was achieved using two Brewster-angle Suprasil 300 blocks with a total path length of 620 mm. We finely adjusted the AOPDF to minimize the pulse duration and suppress the pedestal while monitoring interferometric autocorrelation traces. Figure 24(c) shows the compressed pulse with a duration of 31.7 fs or 4.5 optical cycles. The dispersion is compensated up to the fourth order. The near-field beam profile after the compressor has a clean fundamental mode.

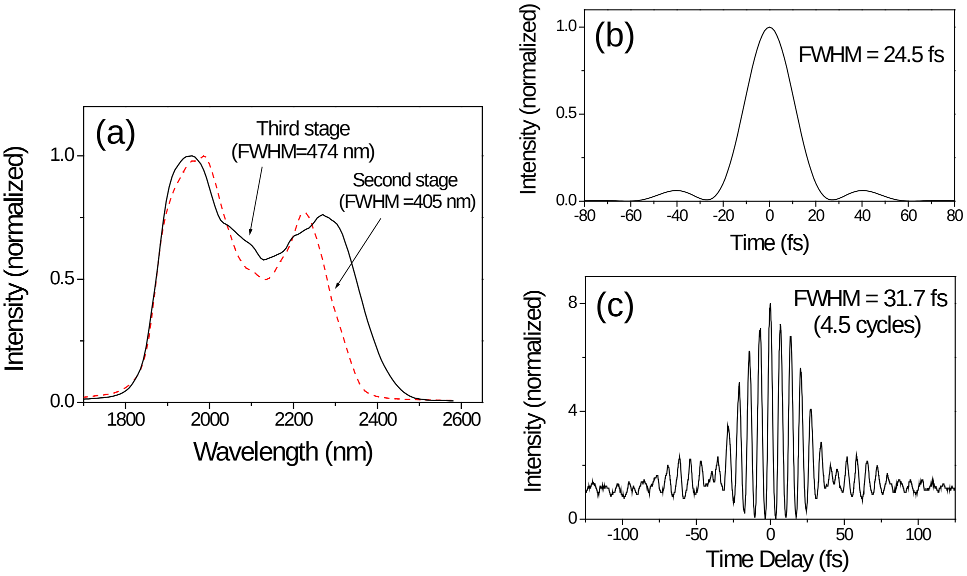

Figure 24. Amplified spectra from the second and third stages (a), the transform-limited pulse duration of 3.5 optical cycles supported by the third-stage spectrum, (b) and the measured IAC trace after compression to 4.5 optical cycles (c).

We characterized the stability and noise characteristics of the amplified pulses to identify the energy portion occupied by the amplified SF. First, the shot-to-shot energy fluctuation of the amplified 2.1-μm pulses is measured to be 4.1% (rms). Second, the shot-to-shot intensity fluctuations, calculated by halving the corresponding intensity fluctuations of low-conversion second harmonic generation (SHG) of the 2.1-μm pulses, are 3.9% (rms). Third, the shot-to-shot fluctuations of the unseeded SF are ~23%. Based on the three stability parameters given above, we can estimate the SF noise to be ~9% from a simple statistical treatment[19]. This means that the signal energy in the main pulse is ~0.77 mJ out of 0.85 mJ. Compared to the parameters in the similar work by Gu *et al* [43], *i.e.*, 9% energy fluctuation and 20% SF noise with 0.74 mJ of compressed pulse energy, our system demonstrates twice better noise performance with a slightly higher compressed pulse energy.

It has already been well proven that intra-pulse DFG generates passively CEP-stabilized pulses. To confirm the CEP-stable operation of our OPCPA system, we measured the shot-to-shot CEP jitter using an *f*-3*f* spectral interferometer where the third-harmonic generation and the self-phase modulated signal is self-referenced with a fixed time delay in the spectral domain. The CEP jitter, measured after the second stage and a compressor, is 195 mrad in 30 s, revealing good CEP stability of the passively stabilized pulses after amplification.

C. HHG experiments using the 2.1-μm OPCPA

The ultimate goal of this OPCPA development is to achieve high-flux HHG in high photon energy range (100-400 eV) for attosecond pulse generation in combination with few-cycle 800-nm OPCPA-driven HHG. As a first step to show the feasibility of achieving this goal, we started HHG experiments in Xe, Kr, and Ar, which are relatively heavy noble gases with low saturation intensities at around 10^{14} W/cm^2. Even though He and Ne are more suitable for HHG with high photon energy, they have relatively high saturation intensity and require a high pressure of ~10 bars at the interaction region [33].

The 2.1-μm OPCPA output [44] was delivered into our HHG vacuum chamber and focused onto the gas jet using an *f*=200 mm or 250 mm CaF_2 lens. The energy and focal spot were controlled together using an iris before the vacuum chamber. The focused laser intensities were ~1×10^{14} W/cm^2 for Xe and ~2×10^{14} W/cm^2 for Kr and Ar. The HHG signal was first detected with an Al-coated XUV photodiode (AXUV100) after another Al filter with a transmission window of 20–70 eV. After confirming the generation of XUV photons in the Al transmission window, we measured the spectrum using our XUV spectrometer with Al, Be, and Zr filters. The measured HHG spectra from Xe, Kr, and Ar are shown in Figs. 25(a)-(c),

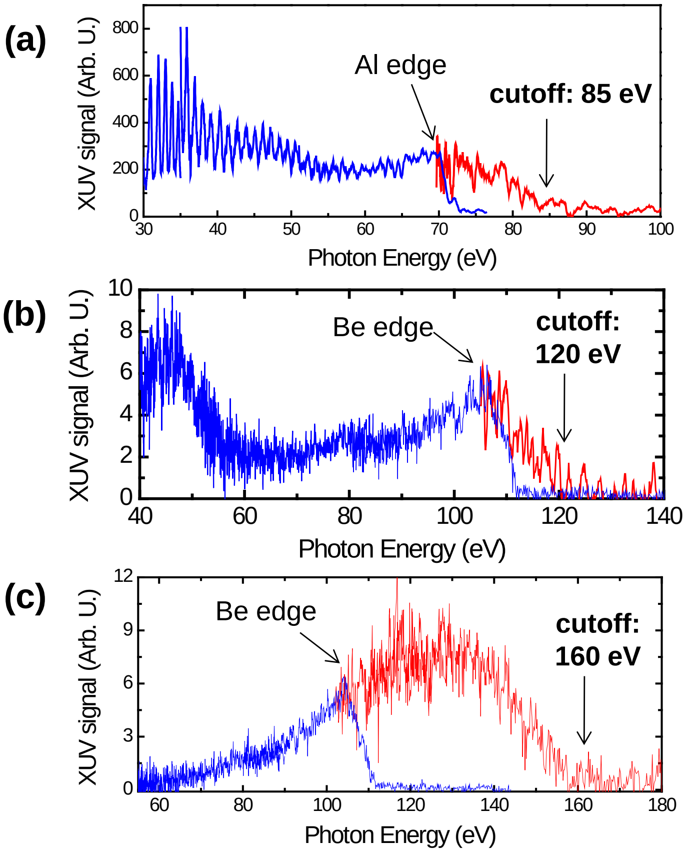

Figure 25. HHG spectrum driven by the kHz, 2.1-μm OPCPA using Xe (a), Kr (b), and Ar (c). The blue line is measured with an Al filter (edge at ~70 eV) or Be filter (edge at ~110 eV) while the red line is measured with a Zr filter. The cutoff energies are ~85 eV for Xe, ~120 eV for Kr, and ~160 eV for Ar.

respectively, where the cutoffs are extended to ~85 eV (~14 nm, ~149th harmonic), ~120 eV (~10 nm, ~211th harmonic) and ~160 eV (~7.8 nm, ~269th harmonic) for each gas.

Compared to the HHG cutoff obtained by a Ti:sapphire laser, these results show a dramatic extension. For example, HHG cutoff in Xe driven by our 35-fs, 800-nm driver is only ~35 eV. We confirmed that the phase matching cutoff is roughly scaled with $\lambda^{1.6\text{-}1.7}$ as known [33]. The HHG efficiency per harmonic of all the cases is measured to be in the range of 10^{-9}–10^{-10}, which is consistent with the wavelength scaling of the HHG efficiency from 10^{-7}–10^{-8} at 90 eV with an 800-nm driver in Ne or He [45].

3.2.b) Upgrade of the 800 nm OPCPA

Section 3.2.a described the upgrade of the 2-micron OPCPA component of the coherent wavelength multiplexer using a cryogenically cooled Yb:YAG amplifier, with the goal of lifting the pulse energy to the millijoule level. Raising the synthesized sub-cycle pulse energy to the millijoule level also requires a pulse energy upgrade to the 800-nm OPCPA component of the wavelength multiplexer. This final step of the upgrade, currently in progress, is described below.

There are two areas of improvement involved in our upgrade of the 800-nm OPCPA to higher pulse energy. First, we are implementing the cryo-Yb:YAG laser system as a pump laser for a newly built third OPA stage, analogous to the upgrade performed in the 2-micron system. Second, since the addition of a third non-collinear OPA stage introduces a new point of high sensitivity to the overlap and relative angle of signal and pump pulses (and at a increased path length from the signal and pump sources), we are implementing changes in the OPCPA design to improve the overall beam pointing stability. These include replacement of the prism pair and grating pair stretchers with compact grism pair stretchers, and replacement of the pump beam SHG stage with a non-critically phase-matched (type 0) LBO crystal with temperature control. Each of these changes will have a significant impact on the third OPA stage performance, as described below.

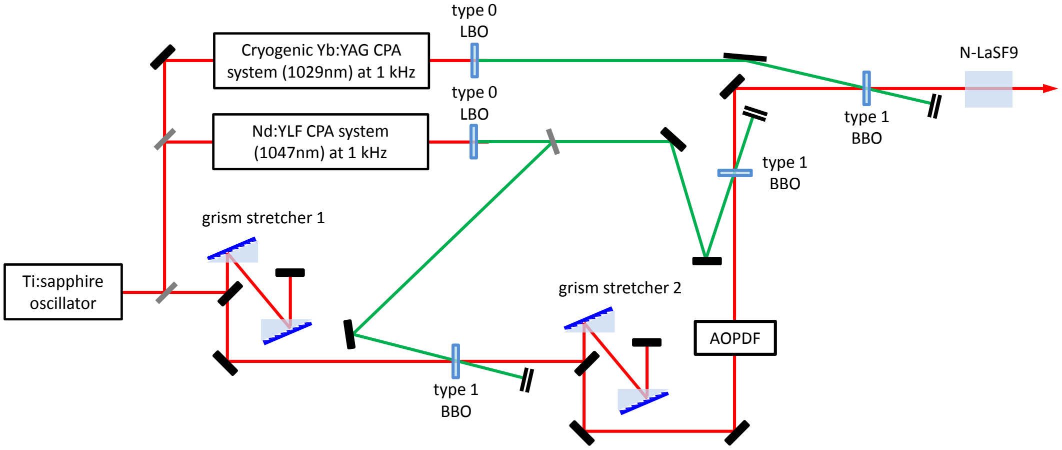

Figure 26. Optical layout of the planned 3-stage 800-nm OPCPA system. The major changes include a 3rd noncollinear OPA stage based on BBO and implementation of the cryo-Yb:YAG laser system to pump this stage. Additionally, two changes in the OPCPA system design are to be implemented for improvement of signal and pump beam pointing stability: replacement of the prism pair and grating pair stretchers with compact grism pair stretchers, and replacement of the pump beam SHG stage with a noncritically phase-matched LBO crystal with temperature control.

The schematic of the planned system is depicted in Fig. 26. In an analogous approach to the upgraded 2-micron OPCPA system (see Fig. 3.2.2), the first two OPA stages will remain pumped by the second harmonic of the Nd:YLF pump laser system, while the new third OPA stage will employ the second harmonic of the cryo-Yb:YAG laser system. Since BBO has an excellent damage threshold, the same crystal design (type-I noncollinear BBO) may be employed, with just a slight change in noncollinear angle to accommodate the change in pump wavelength from 524 nm to 515 nm. This simplifies the design and allows a nearly identical phase-matching bandwidth in the 3rd stage compared with the first two stages. The pump energy available from the cryo-Yb:YAG system is 13 mJ. Our group has previously demonstrated excellent second-harmonic generation conversion efficiency using the 1030-nm Yb:YAG laser pulses to pump a non-critically phase-matched LBO crystal [46]. Expecting the same 54% conversion in this case, 7 mJ/pulse at 515 nm wavelength will be available for pumping the third BBO OPA stage. From this we expect to achieve ~0.7-mJ signal pulses before compression, and ~0.6 mJ after compression to 8 fs in the glass compressor stage.

Use of both the upgraded 2-micron and 800-nm OPCPAs simultaneously will require sharing of the available pump power. Splitting this power equally between OPCPAs, we expect ~0.3 mJ per compressed signal pulse, for a total synthesized waveform energy of ~0.5 mJ after combination of pulses in an Indium Tin Oxide (ITO) dichroic mirror (cut-off wavelength at 1.2 microns).

Fig. 26 also illustrates the inclusion of the new design elements to be implemented for the sake of beam pointing stability. First, the prism pairs employed to stretch the 800-nm seed pulse to 5-ps duration prior to the first OPA stage have been replaced by a grism pair stretcher. The homemade grism design consists of a combined gold-coated grating (200g/mm) and a BK7 glass prism (see design diagram, Fig. 27). By using this grating/prism combination with 1-mm spacing between elements, we are able to obtain a custom grism optic while avoiding the difficulties in manufacturing a grism with the grating etched directly onto the face of a prism. The advantage of using a grism pair rather than a prism pair is a huge increase in compactness. Whereas the prism spacing required for chirping the signal pulse to 5 ps was ~0.5 m, the distance required between grisms needed to provide an equivalent amount of chirp is only ~5 cm. This order-of-magnitude decrease of path length in an optical setup involving multiple angular diffractions provides a huge improvement in the pointing stability of the stretched signal beam. Likewise, we also replaced the grating stretcher between the first two OPA stages (used to further stretch the signal pulses to 6 ps) with a grism pair of the same design. The new dispersion management system, including 2 grism pairs, an AOPDF, and a bulk glass compressor, allows compression of the amplified 800-nm pulses to within 10% of transform limit with compact geometry in each element for superior beam pointing stability.

Finally, by replacing the Type-I critically phase-matched LBO crystal (used in the old 800-nm OPCPA design for doubling the frequency of the 1-micron pump lasers), with a Type-0 non-critically phase-matched LBO crystal, instabilities in pump beam pointing caused by temperature fluctuations in the heavily loaded crystal will be decreased by a factor of two. Moreover, the implementation of a temperature stabilizer in the LBO crystal mount should significantly reduce the pointing instability effect.

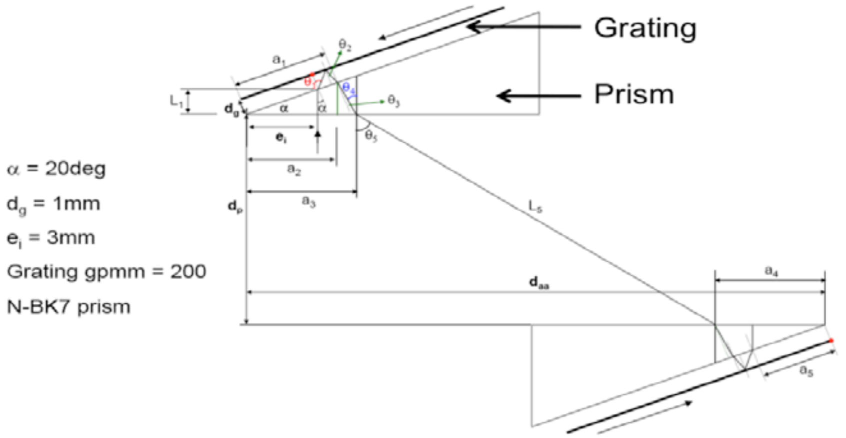

Figure 27. Design of the grism pairs used to achieve compact stretching in the upgraded version of the 800-nm OPCPA. The design pairs a 200g/mm grating with a BK7 glass prism, separated by 1 mm.

3.2.c) Towards efficient seeding of broadband, multicolor parametric amplifiers by means of adiabatic difference frequency conversion

Wavelength multiplexing schemes that coherently synthesize few-cycle OPA pulses of several colors to generate high-energy sub-cycle waveforms, like the one demonstrated in this program, require a multiple-octave-spanning seed spectrum. The approach used in Section 1 to simultaneously cover the 800-nm and 2-micron ranges with broadband spectra was to directly seed the 800-nm OPCPA with the Ti:sapphire (Ti:S) oscillator pulse, and to use intrapulse difference frequency generation (DFG) to mix 690-nm and 950-nm components of the Ti:S pulse to generate a broadband (~1/3-octave) seed for the 2-micron OPCPA. While this method was adequate for the application, intrapulse DFG suffers from poor efficiency, largely a result of the tight focusing and transform-limited duration needed to reach an intensity high enough for nonlinear interaction in the conversion crystal, resulting in a short interaction length. The 2-micron DFG pulse used to seed our 2-micron OPCPA was just a few pJ in energy, less than 1% of the Ti:S power. This low seed power level will likely limit future scaling of the 2-micron OPCPA system to the multi-mJ energy level, since the low seed energy in such high-gain amplifiers results in strong superfluorescence noise contamination, effectively limiting the overall amplifier gain [47]. In the Yb:YAG-pumped, sub-mJ, 2-micron system reported above, the superfluorescence noise energy content of the amplified pulses already approached 10% [44].

A second deficiency of the intrapulse DFG seeding approach is the limited bandwidth of the obtainable DFG pulse, which varies by DFG color. This limitation is governed by the dispersion of nonlinear crystals, which in turn determines the phase-matching bandwidth of any given targeted DFG wavelength. This is important point, given the tremendous potential of the OPA-based wavelength multiplexing concept to allow amplified pulses coherently covering many octaves of bandwidth.

Here we report a major advance towards the seeding of a multiple-octave-spanning coherent wavelength multiplexer, based on the new concept of adiabatic frequency conversion. Adiabatic frequency conversion applies the principle of rapid adiabatic passage (RAP) for full transfer of population between states of a 2-level atom to optical frequency conversion, a concept explored recently in several works [48–50]. Notably, in the mixing of frequencies, ω_3 (idler) = ω_1 (signal)

– ω_2 (pump), where $\omega_1 > \omega_2$, ω_3, through a quadratic electric susceptibility, the equations of motion are isomorphic to the driven optical Bloch equations for a 2-level atom (neglecting radiative losses) when the wave of frequency ω_2 is strong and undepleted during propagation [6–8]. As a result, full photon transfer from ω_1 to ω_3 can be achieved by setting the inital ω_2 wave intensity much greater than the initial ω_1 intensity and by longitudinally and slowly sweeping the wave-vector mismatch of the three-wave mixing process through zero from one sign to the other. This is done by the use of a quasi-phase-matched nonlinear grating with linearly varying poling period.

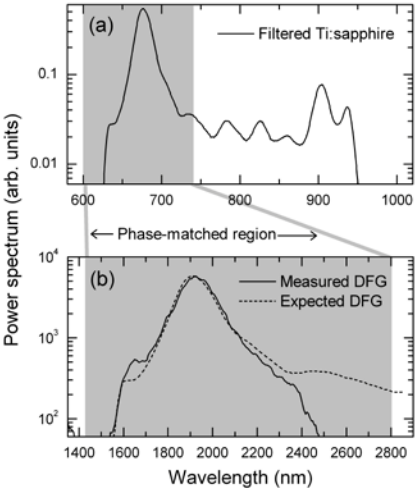

Figure 28. Ti:sapphire spectrum before (a), and after (b) an adiabatic DFG stage, with nearly 100% one-to-one conversion of NIR to MIR photons. Conversion beyond 2.4 μm could not be detected due to the limited sensitivity of the InGaAs spectrometer.

In our application of the adiabatic DFG method to the broadband conversion of a Ti:S oscillator pulse, we employed a powerful 1-μm pump wave to convert a band of the Ti:sapphire NIR pulse to the MIR. We used a small fraction of the 1047-nm Nd:YLF CPA pulses used to pump our OPCPAs, amounting to a few hundred microjoules, as the DFG pump. With a dichroic mirror, we combined this collinearly with the 630-740-nm band of the Ti:S oscillator, which was stretched to 7.3 ps to avoid signal-idler group-velocity walkoff. These were sent to a 20-mm aperiodically poled potassium titanyl phosphate (APKTP) crystal. With high enough 1-μm pump laser intensity (>1 GW/cm^2) we measured the photon number conversion efficiency to be 95% [51], and this result was insensitive to variations in the signal intensity and also to pump intensities above 1 GW/cm^2, allowing near 100% conversion over the full spatial and temporal extents of the signal beam and pulse. Examining the spectra, we demonstrated one-to-one conversion of Ti:S frequencies (630-720 nm) to the 1550-2450 nm range (see Fig. 28).

The scheme used here is immediately suited for the seeding of our 2-micron OPCPA, and the resulting ~100-pJ DFG pulse energy is 2 orders of magnitude higher than that achieved by the intrapulse DFG method. Moreover, our simulations show that lithium niobate, with a transparency window spanning >4 μm, can simultaneously phase match conversion in the 1.5-5 μm range and produce a multi-octave spanning DFG pulse, also with full photon conversion efficiency from Ti:S to DFG. The adiabatic DFG technique is therefore potentially a powerful seeding source for coherent wavelength multiplexers based on OPA.

III. Conclusion

The MIT Single-Cycle Pulse and Isolated Attosecond Pulse Generation Program enabled to demonstrate, for the first time, a novel pulse synthesis technology based on ultrabroadband multi-color OPCPAs and explore the generation and control of isolated attosecond XUV pulses using the synthesized pulses. Under this grant, we developed several relevant ultrafast laser technologies and attosecond measurement systems, such as picosecond cryo-cooled Yb:YAG pump laser amplifiers, 2D and 4DSI pulse characterization techniques, optical balanced cross-correlator, CEP-jitter measurement apparatus, adiabatic DFG technique for high-energy broadband seeding, and a FROG-CRAB setup for attosecond XUV pulse characterization. Experimental demonstration of HHG with the 2.1 μm source shows cutoff extension in Ar to 160 eV and promises the feasibility of coherent sub-cycle control of the HHG process with the synthesized sub-cycle electric-field transients after a further upgrade of the 800-nm OPCPA to the mJ level , as supported by our theoretical study. Since the scaling of energy and pulse duration is clearly possible by using higher-energy OPCPA pump lasers and/or by coherently adding different color OPCPA systems, we believe that the high-energy pulse synthesis technology demonstrated under this grant has opened up a new high-energy ultrafast laser technology that is especially suited to attosecond and strong-field science.

IV. Publications and Patent applications supported by this project:

Archival publications during reporting period (Mar. 2009 - Feb. 2012):

<Journal paper>

1) J. Moses, C. Manzoni, S-W Huang, G.Cerullo, and F. X. Kärtner, “Temporal Optimization of Ultrabroadband High-Energy OPCPA,” Opt. Express **17**, 5540 (Mar, 2009).
2) J. Moses, S.-W. Huang, K.-H. Hong, O. D. Mücke, E. L. Falcão-Filho, A. Benedick, F. Ö. Ilday, A. Dergachev, J. A. Bolger, B. J. Eggleton, and F. X. Kärtner, “Highly stable ultrabroadband mid-IR optical parametric chirped-pulse amplifier optimized for superfluorescence suppression,” Opt. Lett. **34**, 1639 (June, 2009).
3) E. L. Falcão-Filho, V. M. Gkortsas, A. Gordon and F. X. Kärtner, “Analytic scaling of high harmonic generation conversion efficiency,” Opt. Express **17**, 11217 (June, 2009).
4) Kyung-Han Hong, Chien-Jen Lai, Aleem Siddiqui, and Franz X. Kärtner, “130-W picosecond green laser based on a frequency-doubled hybrid cryogenic Yb:YAG amplifier,” Opt. Express **17**, 16911-16919 (Sept, 2009).
5) K.-H. Hong, J. T. Gopinath, D. Rand, A. M. Siddiqui, S.-W. Huang, E. Li, B. J. Eggleton, J. D. Hybl, T. Y. Fan, and F. X. Kärtner, “High-energy, kHz-repetition-rate, ps cryogenic Yb:YAG chirped-pulse amplifier,” Opt. Lett. **35**, 1752 (June, 2010).
6) E. L. Falcão-Filho, C.-J. Lai, K.-H. Hong, V.-M. Gkortsas, S.-W. Huang, L.-J. Chen, and F. X. Kärtner, “Scaling of high-order harmonic efficiencies with visible wavelength drivers: a route to efficient EUV sources,” Appl. Phys. Lett. **97**, 061107 (Aug., 2010).
7) V.-M. Gkortsas, S. Bhardwaj, E. L. Falcão-Filho, K.-H. Hong, A. Gordon and F. X. Kärtner, “Scaling of high harmonic generation conversion efficiency,” J. Phys. B: At. Mol. Opt. Phys. **44,** 045601 (Jan., 2011).
8) Jeffrey Moses and Shu-Wei Huang, “Conformal profile theory for performance scaling of ultrabroadband optical parametric chirped pulse amplification,” J. Opt. Soc. Am. B **28**, 812 (Apr., 2011).
9) Vasileios-Marios Gkortsas, Siddharth Bhardwaj, Chien-Jen Lai, Kyung-Han Hong, Edilson L. Falcão-Filho and Franz X. Kärtner, “Interplay of mulitphoton and tunneling ionization in short-wavelength-driven high-order harmonic generation,” Phys. Rev. A **84**, 013427 (July 29, 2011).
10) Shu-Wei Huang, Giovanni Cirmi, Jeffrey Moses, Kyung-Han Hong, Siddharth Bhardwaj, Jonathan R. Birge, Li-Jin Chen, Enbang Li, Benjamin Eggleton, Giulio Cerullo, and Franz X. Kärtner, “High-energy pulse synthesis with sub-cycle waveform control for strong-field physics,” Nature Photonics **5**, 475-479 (Aug. 1, 2011).
11) Kyung-Han Hong, Shu-Wei Huang, Jeffrey Moses, Xing Fu, Chien-Jen Lai, Giovanni Cirmi, Alexander Sell, Eduardo Granados, Phillip Keathley, and Franz X. Kärtner, “High-energy,

phase-stable, ultrabroadband kHz OPCPA at 2.1 μm pumped by a picosecond cryogenic Yb:YAG laser," Opt. Express **19**, 15538-15548 (Aug. 1, 2011).

12) Chen-Jen Lai and Franz X. Kärtner, "The influence of plasma defocusing in high harmonic generation," Opt. Express **19**, 22377-22387 (Oct., 2011).
13) Jeffrey Moses, Haim Suchowski, and Franz X. Kärtner, "Fully efficient adiabatic downconversion of broadband Ti:sapphire oscillator pulses," Opt. Lett., in press (2012).
14) Shu-Wei Huang, Giovanni Cirmi, Jeffrey Moses, Kyung-Han Hong, Siddharth Bhardwaj, Jonathan R. Birge, Li-Jin Chen, Irina V. Kabakova, Enbang Li, Benjamin J. Eggleton, Giulio Cerullo, and Franz X. Kärtner, "Optical waveform synthesizer and its application to high-harmonic generation," J. Phys. B, in press (2012).

<Submitted >

A.1) Eduardo Granados, Li-Jin Chen, Chien-Jen Lai, Kyung-Han Hong, and Franz X. Kärtner, "Wavelength scaling of optimal hollow-core fiber compressors in single-cycle limit," Optics Express, submitted (Dec. 15, 2011).

A.2) Giovanni Cirmi, Chien-Jen Lai, Shu-Wei Huang, Eduardo Granados, Kyung-Han Hong, Jeffrey Moses, Phillip Keathley, Alexander Sell, and Franz X. Kärtner, "Tunable high-harmonic generation driven by a femtosecond visible optical parametric amplifier," J. Physics B, to be submitted (2012).

<Conference paper>

15) E. L. Falcão-Filho, V. M. Gkortsas, A. Gordon and F. X. Kärtner, "Conversion efficiency, scaling and global optimization of high harmonic generation," Conference on Lasers and Electro Optics (CLEO), Baltimore, MD, June 1-5, 2009.
16) K.-H. Hong, J. Gopinath, A. Siddiqui, J. Moses, C.-J. Lai, J. Hybl, and T. Y. Fan, "High-average-power cryogenically-cooled picosecond Yb:YAG amplifier seeded by a fiber CPA system," Conference on Lasers and Electro Optics (CLEO), Baltimore, MD, June 1-5, 2009 (invited).
17) S.-W. Huang, J. Moses, K.-H. Hong, E. L. Falcao-Filho, A. Benedick, J. A. Bolger, B. J. Eggleton, and F. X. Kärtner, "High-Power, Few-Cycle, Phase-Stabilized 2.2-μm Optical Parametric Chirped Pulse Amplifier," Conference on Lasers and Electro Optics (CLEO), Baltimore, MD, June 1-5, 2009.
18) J. Moses, C. Manzoni, S-W Huang, G.Cerullo, and F. X. Kärtner, "Multi-Stage Optimization of Ultrabroadband High-Energy Optical Parametric Chirped Pulse Amplification," Conference on Lasers and Electro Optics (CLEO), Baltimore, MD, June 1-5, 2009.
19) F. X. Kärtner, "High Power Ultrafast Laser Systems for EUV and X-ray Sources," Keynote presented at Directed Energy Professional Society Workshop, Newton, MA, June 30 – July 2, 2009 (invited).
20) F. X. Kärtner, "Octave-Spanning Ti:sapphire Lasers and Carrier-Envelope Phase Control," Conference on Attosecond Science, Kansas State University, Manhattan, KS, July 28 – August 1, 2009 (invited).
21) Shu-Wei Huang, Jeffrey Moses, Kyung-Han Hong, Edilson L. Falcão-Filho, Andrew Benedick, Jeremy Bolger, Benjamin Eggleton, and Franz X. Kärtner, "Highly stable, few-cycle, 2.2-μm optical parametric chirped pulse amplifier," Attosecond Physics 2009 (Kansas State University, Manhattan, Kansas, July 28 – Aug. 1, 2009) T21
22) J. Moses, S.-W. Huang, K.-H. Hong, E. L. Falcão-Filho, A. Benedick, J. Bolger, B. Eggleton, and F. X. Kärtner, "10-GW, 3-optical-cycle, 2.2-μm-wavelength parametric amplifier with high stability," 1st EOS topical meeting on laser (Capri, Italy, Sep. 27-30, 2009) oral presentation.
23) Kyung-Han Hong, Chien-Jen Lai, Aleem Siddiqui, and Franz X. Kärtner, "130-W picosecond green light from a frequency-doubled hybrid cryogenic Yb:YAG laser system,"

UFO/HFSW 2009 (Arcachon, France, Aug. 31-Sept. 4, 2009), Tuesday oral presentation.

24) F. X. Kärtner, Tutorial on “Carrier-Envelope Phase Controlled Laser Systems, Conference on Ultrafast Optics and High Fields Short Wavelength,” (UFO VII – HFSW XIII), Arcachon, France, August 31 – September 4, 2009 (invited).
25) Kyung-Han Hong, Juliet Gopinath, Darren Rand, Aleem Siddiqui, Shu-Wei Huang, Enbang Li, Benjamin Eggleton, John Hybl, Tso Yee Fan, and Franz X. Kärtner, “Generation of 2-kHz, 40-mJ Picosecond Pulses from a Cryogenic Yb:YAG Chirped-Pulse Amplifier for OPCPA Pumping,” ASSP 2010 (San Diego, 2010), post-deadline paper APDP1.
26) Shu-Wei Huang, Giovanni Cirmi, Jeffrey Moses, Kyung-Han Hong, Andrew Benedick, Li-Jin Chen, Enbang Li, Benjamin Eggleton, Giulio Cerullo and Franz X. Kärtner, “Ultrabroadband Optical Parametric Chirped Pulse Amplifier System for Single-Cycle Waveform Synthesis,” CLEO/QELS 2010 (San Jose, May 16-21, 2010) CWA4.
27) Edilson L. Falcão-Filho, Chien-Jen Lai, Vasileios-Marios Gkortsas, Shu-Wei Huang, Li-Jin Chen, Kyung-Han Hong, and Franz X. Kärtner, “Scaling of high harmonic generation efficiencies with 400-nm and 800-nm driver pulses,” CLEO/QELS 2010 (San Jose, May 16-21, 2010) JThI4.
28) Kyung-Han Hong, Juliet Gopinath, Darren Rand, Aleem Siddiqui, Shu-Wei Huang, Enbang Li, Benjamin Eggleton, John Hybl, Tso Yee Fan, and Franz X. Kärtner, “High-energy, picosecond, cryogenic Yb:YAG chirped-pulse amplifier at kHz repetition rates for OPCPA pumping,” CLEO/QELS 2010 (San Jose, May 16-21, 2010) JThD2.
29) J. Moses, S.W. Huang and F.X. Kärtner, “Performance Scaling of Ultrabroadband OPCPA with Conformal Pulse Profiles,” CLEO/QELS 2010, San Jose, CA, May 2010.
30) Shu-Wei Huang, Giovanni Cirmi, Jeffrey Moses, Kyung-Han Hong, Andrew Benedick, Li-Jin Chen, Enbang Li, Benjamin Eggleton, Giulio Cerullo, and Franz X. Kärtner, “Scalable High-Energy Sub-Cycle Waveform Synthesis,” Ultrafast Phenomena 2010 (Snowmass village, Colorado, July 18-23), postdeadline paper, PDP1.
31) E. L. Falcão-Filho, C.-J. Lai, V.-M. Gkortsas, S.-W. Huang, L.-J. Chen, K.-H. Hong, and F. X. Kärtner, “High Efficiency High Harmonic Generation Based EUV Sources,” Laser Physics Workshop 2010 (Foz do Iguacu, Brazil, July 5-9, 2010) Sem. 5.4.4.
32) V.- M. Gkortsas, C.-J. Lai, E. L. Falcão-Filho, K.-H. Hong, S. Bhardwaj, S.-W. Huang, L.-J. Chen and F. X. Kärtner, “Scaling of high-order harmonic efficiencies with visible wavelength drivers: a route to efficient EUV sources,” Gordon Research Conference on Multiphoton Processes (Tilton School, New Hampshire, June 6-11, 2010) poster session.
33) Shu-Wei Huang, Giovanni Cirmi, Jeffrey Moses, Kyung-Han Hong, Andrew Benedick, Li-Jin Chen, Enbang Li, Benjamin Eggleton, Giulio Cerullo and Franz X. Kärtner, “Ultrabroadband Optical Parametric Chirped Pulse Amplifier System for Single-Cycle Waveform Synthesis,” Gordon Research Conference on Multiphoton Processes (Tilton School, New Hampshire, June 6-11, 2010) poster session.
34) Shu-Wei Huang, Giovanni Cirmi, Kyung-Han Hong, Jeffrey Moses, Jonathan R. Birge, Siddharth Bhardwaj, Vasileios-Marios Gkortsas, Andrew Benedick, Li-Jin Chen, Enbang Li, Benjamin Eggleton, Giulio Cerullo, and Franz X. Kärtner, “Scalable High-Energy Sub-Cycle Waveform Synthesis for High-Field Physics,” High Intensity Lasers and High Field Phenomena 2011 (HILAS, Feb. 16-18, 2011), JWC4.
35) C. J. Lai and F. X. Kärtner, “Plasma Defocusing in High Harmonic Generation with Long-Wavelength Driver Pulses,” High Intensity Lasers and High Field Phenomena 2011 (HILAS, Feb. 16-18, 2011), HThC4.
36) Kyung-Han Hong, Shu-Wei Huang, Jeffrey Moses, Xing Fu, Chien-Jen Lai, Giovanni Cirmi, and Franz X. Kärtner, “High-energy, Ultrabroadband, kHz OPCPA at 2.1 μm Pumped by a *ps* Cryogenic Yb:YAG chirped-pulse amplifier,” 1st CFEL international symposium 2011 (Sylt, Germany, Mar. 18-20, 2011), invited session.
37) P. Keathley, A. Soane, C. Lai, J. Moses, and F. X. Kärtner, “Frequency Resolved Optical

Gating of Attosecond Pulses," 1st CFEL international symposium 2011 (Sylt, Germany, Mar. 18-20, 2011), poster session.

38) C. Manzoni, J. Moses, F.X. Kärtner and G. Cerullo "The Evolution of Signal-to-noise Ratio on Superfluorescence-contaminated Optical Parametric Chirped Amplification," Ultrafast Phenomena 2010 (Snowmass village, Colorado, July 18-23), poster session.
39) Vasileios-Marios Gkortsas, Chien-Jen Lai, Kyung-Han Hong, Siddharth Bhardwaj, Edilson L Falcão-Filho and Franz X. Kärtner, "Influence of Nonadiabatic Tunneling Ionization on Short-Wavelength-Driven High Harmonic Generation," CLEO/QELS 2011 (Baltimore, Maryland, May 1- May 6, 2011) JThB48.
40) Kyung-Han Hong, Shu-Wei Huang, Jeffrey Moses, Xing Fu, Chien-Jen Lai, Giovanni Cirmi, and Franz X. Kärtner, "High-energy, Ultrabroadband, kHz OPCPA at 2.1 μm Pumped by a ps Cryogenic Yb:YAG chirped-pulse amplifier," 1st CFEL international symposium 2011 (Sylt, Germany, Mar. 18-20, 2011).
41) Kyung-Han Hong, Shu-Wei Huang, Jeffrey Moses, Xing Fu, Chien-Jen Lai, and Franz X. Kärtner, "High-energy, Few-cycle, kHz OPCPA at 2.1 μm Pumped by a Picosecond Cryogenic Yb:YAG Laser," CLEO/QELS 2011 (Baltimore, Maryland, May 1-6, 2011) CTuT3.
42) J. Moses, C. Manzoni, G. Cerullo, and F. X. Kärtner, "Superfluorescence Dynamics of OPCPAs in the Saturation Regime," CLEO Europe 2011.
43) K.-H. Hong, S.-W. Huang, J. Moses, X. Fu, G. Cirmi, C.-J. Lai, S. Bhardwaj, and F. X. Kärtner, "CEP-stable, few-cycle, kHz OPCPAs for attosecond science: Energy scaling and coherent sub-cycle pulse synthesis," ATTO3 (Sapporo, Japan, July 6-8, 2011) poster 39.
44) C. J. Lai, K.-H. Hong, and F. X. Kärtner, "Plasma defocusing in high harmonic generation," ATTO3 (Sapporo, Japan, July 6-8, 2011) poster 21.
45) Kyung-Han Hong, Shu-Wei Huang, Jeffrey Moses, Xing Fu, Chien-Jen Lai, Giovanni Cirmi, Alexander Sell, Eduardo Granados, Phillip Keathley, and Franz X. Kärtner, "High-energy, kHz, 2.1-μm OPCPA pumped by a cryogenic Yb:YAG laser and its application to high harmonic generation," Ultrafast Optics VIII (Monterey, CA, Sept. 25-30, 2011) oral presentation We10.
46) J. Moses, S.-W. Huang, D. Keathley, G. Cirmi, K.-H. Hong, S. Bhardwaj, A. Sell, C. J. Lai, V.-M. Gkortsas, and F. X. Kärtner, "Towards Two-Color Attosecond XUV/Mid-IR Photoion and Photoelectron Spectroscopy Using a Coherent Wavelength Multiplexer," Gordon Research Conference on Photoions, Photoionization & Photodetachment, Galveston, TX, February 2012.
47) J. Moses, F. X. Kärtner, and H. Suchowski, "Rapid adiabatic passage in nonlinear optics for complete power transfer between ultrabroadband optical pulses," APS March Meeting 2012.

- Patent

Franz X. Kaertner, Edilson L. Falcao-Filho, Chien-Jen Lai, Kyung-Han Hong, and Tso Yee Fan, "Efficient High-Harmonic-Generation-Based EUV Source Driven by Short Wavength Light," USA application number 61/286,347 (filed Dec. 14, 2009, pending), publication number US 2011/0140009 (Jun. 16, 2011).

References

1. E. Goulielmakis, M. Schultze, M. Hofstetter, V. S. Yakovlev, J. Gagnon, M. Uiberacker *et al.* "Single-Cycle Nonlinear Optics," Science **320**, 1614 (2008).
2. F. Krausz and M. Ivanov, "Attosecond physics," Rev. Mod. Phys. **81**, 163 (2009).
3. L. E. Chipperfield, J. S. Robinson, J. W. G. Tisch, and J. P. Marangos, "Ideal Waveform to Generate the Maximum Possible Electron Recollision Energy for Any Given Oscillation Period," Phys. Rev. Lett. **102**, 063003 (2009).
4. A. Dubietis, R. Butkus R, and A. P. Piskarskas, "Trends in chirped pulse optical parametric amplification," IEEE J. Sel. Top. Quant. **12**, 163 (2006).
5. T. R. Schibli, J. Kim, O. Kuzucu, J. T. Gopinath, S. N. Tandon, G. S. Petrich *et al.* “Attosecond active synchronization of passively mode-locked lasers by balanced cross correlation,” Opt. Lett. **28,** 947 (2003).
6. T. Miura, K. Kobayashi, K. Takasago, Z. Zhang, K. Torizuka, and F. Kannari, “Timing jitter in a kilohertz regenerative amplifier of a femtosecond-pulse Ti:Al_2O_3 laser,” Opt. Lett. **25,** 1795 (2000).
7. Z. Chang, “Carrier-envelope phase shift caused by grating-based stretchers and compressors,” Appl. Opt. **45,** 8350 (2006).
8. Q. Zou, and B. Lü, “Propagation properties of ultrashort pulsed beams with constant waist width in free space,” Opt. Laser Technol. **39,** 619 (2007).
9. J. R. Birge, H. M. Crespo, and F. X. Kärtner, “Theory and design of two-dimensional spectral shearing interferometry for few-cycle pulse measurement,” J. Opt. Soc. Am. B **27,** 1165 (2010).
10. C. Dorrer, E. M. Kosik, and I. A. Walmsley, “Spatio-temporal characterization of the electric field of ultrashort optical pulses using two-dimensional shearing interferometry,” Appl. Phys. B **74** S209 (2002).
11. S.-W. Huang, G. Cirmi, J. Moses, K.-H. Hong, S. Bhardwaj, J. R. Birge *et al.*, "High-energy pulse synthesis with sub-cycle waveform control for strong-field physics," Nature Photonics **5**, 475 (2011).
12. A. Wirth *et al.*, Science **334**, 195 (2011).
13. A. Baltuska *et al.*, Nature (London) **421**, 611 (2003).
14. E. Priori *et al.*, Phys. Rev. A **61**, 063801 (2000).
15. A. Bohan, P. Antoine, D. Milosevic, and B. Piraux, Phys. Rev. Lett. **81**, 9 (1998).
16. V. M. Gkortsas *et al.*, J.Phys. B. **44**, 045601 (2011).
17. Ferrari F, Calegari F, Lucchini M, Vozzi C, Stagira S, Sansone G *et al.* "High-energy isolated attosecond pulses generated by above-saturation few-cycle fields," Nature Photonics **4**, 875 (2010).
18. Z. Chang, B. Shan, and S. Ghimire S, "Generation of the attosecond extreme ultraviolet supercontinuum by a polarization gating," J. Mod. Opt. **52,** 277 (2005).
19. G. Sansone, E. Benedetti, F. Calegari, C. Vozzi, L. Avaldi, R. Flammini *et al.* "Isolated Single-Cycle Attosecond Pulses," Science **314,** 443 (2006).
20. I. J. Kim, C. M. Kim, H. T. Kim, G. H. Lee, Y. S. Lee, J. Y. Park *et al.* "Highly Efficient High-Harmonic Generation in an Orthogonally Polarized Two-Color Laser Field," Phys. Rev. Lett. **94,** 243901 (2005).
21. Y. Oishi, M. Kaku, A. Suda, F. Kannari, and K. Midorikawa, "Generation of extreme ultraviolet continuum radiation driven by a sub-10-fs two-color field," Opt. Express **14,** 7230 (2006).
22. M. J. Abel, T. Pfeifer, P. M. Nagel, W. Boutu, M. J. Bell, C. P. Steiner *et al.* "Isolated attosecond pulses from ionization gating of high-harmonic emission," Chem. Phys. **366,** 9 (2009).
23. H. Mashiko, S. Gilbertson, C. Li, S. D. Khan, M. M. Shakya, E. Moon *et al.* "Double Optical Gating of High-Order Harmonic Generation with Carrier-Envelope Phase Stabilized Lasers," Phys. Rev. Lett. **100,** 103906 (2008).
24. N. Dudovich, O. Smirnova, J. Levesque, Y. Mairesse, M. Y. Ivanov, D. M. Villeneuve *et al.* "Measuring and controlling the birth of attosecond XUV pulses," Nat Phys. **2** 781 (2006).
25. B. Henke, "X-Ray Interactions: Photoabsorption, Scattering, Transmission, and Reflection at E = 50-30,000 eV, Z = 1-92," At. Data Nucl. Data Tables **54,** 181 (1993).

26. Y. Mairesse and F. Quéré, Phys. Rev. A, **71**, 011401 (2005).
27. K. T. Kim *et al.*, New Journal of Physics **12**, 083019 (2010).
28. A. Gordon and F. X. Kärtner, "Scaling of keV HHG photon yield with drive wavelength," Opt. Express **13**, 2941 (2005).
29. P. Colosimo, G. Doumy, C. I. Blaga, J. Wheeler, C. Hauri, F. Catoire, J. Tate, R. Chirla, A. M. March, G. G. Paulus, H. G. Muller, P. Agostini, and L. F. DiMauro, "Scaling strong-field interactions towards the classical limit," Nat. Physics **4**(5), 386–389 (2008).
30. E. J. Takahashi, T. Kanai, K. L. Ishikawa, Y. Nabakawa, K. Midorikawa, Coherent water window x-ray by phase-matched high-order harmonics, Phys. Rev. Lett. **101**, 253901 (2008).
31. E. L. Falcão-Filho, V. M. Gkortsas, A. Gordon, and F. X. Kärtner, "Analytic scaling analysis of high harmonic generation conversion efficiency," Opt. Express **17**, 11217-11229 (2009),
32. A. D. Shiner, C. Trallero-Herrero, N. Kajumba, H.-C. Bandulet, D. Comtois, F. Légaré, M. Giguère, J-C. Kieffer, P. B. Corkum, and D. M. Villeneuve, "Wavelength Scaling of High Harmonic Generation Efficiency," Phys. Rev. Lett. **103**, 073902 (2009).
33. M. C. Chen, P. Arpin, T. Popmintchev, M. Gerrity, B. Zhang, M. Seaberg, D. Popmintchev, M. M. Murnane, and H. C. Kapteyn, "Ultrafast Soft X-Ray Harmonics Spanning the Water Window from a Tabletop Light Source," Phys. Rev. Lett. **105**, 173901 (2010).
34. Chuang Li, Ding Wang, Liwei Song, Jun Liu, Peng Liu, Canhua Xu, Yuxin Leng, Ruxin Li, and Zhizhan Xu, "Generation of carrier-envelope phase stabilized intense 1.5 cycle pulses at 1.75 μm," Opt. Express **19** (7), 6783-6789 (2011).
35. Bruno E. Schmidt, Andrew D. Shiner, Philippe Lassonde, Jean-Claude Kieffer, Paul B. Corkum, David M. Villeneuve, François Légaré, "CEP stable 1.6 cycle laser pulses at 1.8 μm," Opt. Express **19** (7), 6858 (2011).
36. T. Y. Fan, D. J. Ripin, R. L. Aggarwal, J. R. Ochoa, B. Chann, M. Tilleman, and J. Spitzberg, "Cryogenic Yb^{3+}-Doped Solid-Stae Lasers," IEEE J. Sel. Top. Quantum Electron. **13**, 448 (2007).
37. Y. Akahane, M. Aoyama, K. Ogawa, K. Tsuji, S. Tokita, J. Kawanaka, H. Nishioka, and K. Yamakawa, "High-energy, diode-pumped, picosecond Yb:YAG chirped-pulse regenerative amplifier for pumping optical parametric chirped-pulse amplification," Opt. Lett. **32**, 1899 (2007).
38. K.-H. Hong, A. Siddiqui, J. Moses, J. Gopinath, J. Hybl, F. Ö. Ilday, T. Y. Fan, and F. X. Kärtner, "Generation of 287 W, 5.5 ps pulses at 78 MHz repetition rate from a cryogenically cooled Yb:YAG amplifier seeded by a fiber chirped-pulse amplification system," Opt. Lett. **33**, 2473 (2008).
39. F. J. Furch, B. A. Reagan, B. M. Luther, A. H. Curtis, S. P. Meehan, and J. J. Rocca, "Demonstration of all-diode-pumped soft x-ray laser," Opt. Lett. **34**, 3352 (2009).
40. K.-H. Hong, J. Gopinath, D. Rand, A. Siddiqui, S.-W. Huang, E. Li, B. Eggleton, J. D. Hybl, T. Y. Fan and F. X. Kärtner, "High-energy, kHz-repetition-rate, ps cryogenic Yb:YAG chirped-pulse amplifier," Opt. Lett. **35**, 1752-1754 (2010).
41. T. Metzger, A. Schwarz, C. Y. Teisset, D. Sutter, A. Killi, R. Kienberger, and F. Krausz, "High-repetition-rate picosecond pump laser based on a Yb:YAG disk amplifier for optical parametric amplification," Opt. Lett. **34**, 2123-2125 (2009).
42. J. Moses, S.-W. Huang, K.-H. Hong, O. D. Mücke, E. L. Falcão-Filho, A. Benedick, F. Ö. Ilday, A. Dergachev, J. A. Bolger, B. J. Eggleton, and F. X. Kärtner, "Highly stable ultrabroadband mid-IR optical parametric chirped-pulse amplifier optimized for superfluorescence suppression," Opt. Lett. **34**, 1639-1641 (2009).
43. X. Gu, G. Marcus, Y. Deng, T. Metzger, C. Teisset, N. Ishii, T. Fuji, A. Baltuska, R. Butkus, V. Pervak, H. Ishizuki, T. Taira, T. Kobayashi, R. Kienberger, and F. Krausz, "Generation of carrier-envelope-phase-stable 2-cycle 740-μJ pulses at 2.1-μm carrier wavelength," Opt. Express **17**, 62 (2009).
44. K.-H. Hong, S.-W. Huang, J. Moses, X. Fu, C.-J. Lai, G. Cirmi, A. Sell, E. Granados, P. Keathley, and F. X. Kärtner, "High-energy, phase-stable, ultrabroadband kHz OPCPA at 2.1 μm pumped by a picosecond cryogenic Yb:YAG laser," Opt. Express **19**, 15538-15548 (2011).

45. E. L. Falcão-Filho, C.-J. Lai, K.-H. Hong, V.-M. Gkortsas, S.-W. Huang, L.-J. Chen, and F. X. Kärtner, “Scaling of high-order harmonic efficiencies with visible wavelength drivers: a route to efficient EUV sources,” Appl. Phys. Lett. **97**, 061107 (2010).
46. K.-H. Hong, C.-J. Lai, A. Siddiqui, and F. X. Kärtner, “130-W picosecond green laser based on a frequency-doubled hybrid cryogenic Yb:YAG amplifier,” Opt. Express **17**, 16911-16919 (2009).
47. C. Manzoni, J. Moses, F. X. Kärtner, and G. Cerullo, "Excess quantum noise in optical parametric chirped-pulse amplification," Opt. Express **19**, 8357-8366 (2011).
48. H. Suchowski, D. Oron, A. Arie, and Y. Silberberg, "Geometrical representation of sum frequency generation and adiabatic frequency conversion," Phys. Rev. A **78**, 063821 (2008).
49. H. Suchowski, V. Prabhudesai, D. Oron, A. Arie, and Y. Silberberg, "Robust adiabatic sum frequencyconversion," Opt. Express **17**, 12731-12740 (2009).
50. H. Suchowski, B. D. Bruner, A. Ganany-Padowicz, I. Juwiler, A. Arie, and Y. Silberberg, "Adiabatic frequency conversion of ultrafast pulses," Applied Physics B **105**, 697-702 (2011).
51. J. Moses, H. Suchowski, and F. X. Kärtner, Opt. Lett., *in press* (2012).